Assimilation of Flash Extent Data in the Variational Framework at Convection-Allowing Scales: Proof-of-Concept and Evaluation for the Short-Term Forecast of the 24 May 2011 Tornado Outbreak

ALEXANDRE O. FIERRO

Cooperative Institute for Mesoscale Meteorological Studies, University of Oklahoma, and NOAA/OAR/National Severe Storms Laboratory, Norman, Oklahoma

JIDONG GAO AND CONRAD L. ZIEGLER

NOAA/National Severe Storms Laboratory, Norman, Oklahoma

KRISTIN M. CALHOUN

Cooperative Institute for Mesoscale Meteorological Studies, University of Oklahoma, and NOAA/OAR/National Severe Storms Laboratory, Norman, Oklahoma

EDWARD R. MANSELL AND DONALD R. MACGORMAN

NOAA/National Severe Storms Laboratory, Norman, Oklahoma

(Manuscript received 5 February 2016, in final form 4 August 2016)

ABSTRACT

This work evaluates the performance of the assimilation of total lightning data within a three-dimensional variational (3DVAR) framework for the analysis and short-term forecast of the 24 May 2011 tornado outbreak using the Weather Research and Forecasting (WRF) Model at convection-allowing scales. Between the lifted condensation level and a fixed upper height, pseudo-observations for water vapor mass first are created based on either the flash extent densities derived from Oklahoma Lightning Mapping Array data or the lightning source densities derived from the Earth Networks pulse data, and then assimilated by the 3DVAR system. Assimilation of radar data with 3DVAR and a cloud analysis algorithm (RAD) also are performed as a baseline for comparison and in tandem with lightning to evaluate the added value of this lightning data assimilation (LDA) method.

Given a scenario wherein the control experiment without radar or lightning data assimilation fails to accurately initiate and forecast the observed storms, the LDA and RAD yield comparable short-term forecast improvements. The RAD alone produces storms of similar strength to the observations during the first 30 min of forecast more rapidly than the LDA alone; however, the LDA is able to better depict individual supercellular features at 1-h forecast. When both the lightning and radar data are assimilated, the 30-min forecast showed noteworthy improvements over RAD in terms of the model's ability to better resolve individual supercell structures and still maintained a 1-h forecast similar to that from the LDA. The results chiefly illustrate the potential value of assimilating total lightning data along with radar data.

1. Introduction

Given the potential threat to life and property posed annually by high-impact weather events such as flash floods, hail, tornadoes and lightning, it is critical to provide timely, accurate forecasts of these events. While forecasts of severe weather have improved in recent years, forecasting these events at the cloud scale with desired timeliness and accuracy still remains a challenge, because it involves resolving nonlinear interactions among many different physical processes over a large range of scales (e.g., Stensrud et al. 2009). Various methods of data assimilation have been developed using multiple data sources to try to improve forecasts and reduce false alarms (e.g., Park and Xu 2013).

Corresponding author address: Alexandre O. Fierro, CIMMS, National Weather Center, Suite 2100, 120 David L. Boren Blvd., Norman, OK 73072.
E-mail: alex.fierro@noaa.gov

DOI: 10.1175/MWR-D-16-0053.1

Much of the data assimilation research thus far has examined assimilation of various observations of deep convection, especially from the National Weather Service (NWS) operational Weather Surveillance Radar–1988 Doppler (WSR-88D) (e.g., Evensen 1994, 2003; Houtekamer and Mitchell 1998; Zhang 2005; Zhang et al. 2009; Aksoy et al. 2009; Godinez et al. 2012). In some areas of the United States, however, coverage by the WSR-88D network is poor or absent (e.g., Zhang et al. 2011). This is the case especially in mountainous terrain having beam blockage and in oceanic regions beyond the range of coastal radars. In these circumstances, lightning mapping data can serve as an indicator of deep moist convection for assimilation into numerical weather prediction models. Recent works (Mansell et al. 2007; Fierro et al. 2012a, hereafter F12a; Fierro et al. 2014, hereafter F14; Fierro et al. 2015, hereafter F15; Mansell 2014) demonstrated that assimilating lightning data improves short-term forecasts as much as assimilating radar reflectivity does. In areas in which the spatiotemporal coverage of the WSR-88D network is good, however, the added value of lightning data assimilation (LDA) to forecasts based on assimilating radar data is not yet well established. Surface lightning detection networks already provide good coverage in many regions with poor radar coverage, and the Geostationary Lightning Mapper (GLM; Goodman et al. 2013) on board the Geostationary Operational Environmental Satellite "R" series (GOES-R; Gurka et al. 2006; Goodman et al. 2013), planned for launch in fall 2016, provides additional coverage over land and oceans. Thus, incorporating lightning data substantially extends the uniformity and range of coverage for assimilating a measure of deep convection.

Thus far, relatively few data assimilation studies have devoted their attention to lightning data. Most LDA studies have employed data from lightning mapping systems that detected mostly cloud-to-ground (CG) flashes and used mesoscale models with parameterized convection (i.e., Jones and Macpherson 1997a,b; Alexander et al. 1999; Chang et al. 2001; Papadopoulos et al. 2005; Pessi and Businger 2009). Observational studies and storm simulations, however, have both provided considerable evidence that total lightning flash rates are much better correlated than CG flash rates with various measures of intensifying deep convection, such as updraft mass flux and graupel volume (e.g., MacGorman et al. 1989; Carey and Rutledge 1998; MacGorman et al. 2005; Wiens et al. 2005; Kuhlman et al. 2006; Fierro et al. 2006; Deierling and Petersen 2008; MacGorman et al. 2011). Furthermore, intracloud flashes (ICs) generally outnumber CGs by a factor of 2–3 in typical single or multicell thunderstorms (Boccippio et al. 2001) to >10:1 within some severe deep convective storms and supercells (e.g., MacGorman et al. 1989; 190–192 of MacGorman and Rust 1998). Thus, total lightning activity provides a much higher rate of observations and few studies have begun developing techniques for assimilating total lightning into mesoscale models using parameterized convection (Mansell et al. 2007) or using sufficient grid resolution to explicitly allow convection (F12; F14; F15; Marchand and Fuelberg 2014; Mansell 2014; Allen et al. 2016). Generally speaking, these LDA studies have employed an empirical relationship between lightning and other diagnosed quantities, such as rainfall, latent heating, or relative humidity to force or modify parameterized convection at the observed lightning locations.

The approach of the present study is inspired by earlier LDA efforts based on an initial concept put forth in Fierro and Reisner (2011) and subsequently refined in F12a and F14. Both F12a and F14 employed a simple, computationally efficient direct insertion (nudging) method for assimilating total lightning data from the Earth Networks Total Lightning Network (ENTLN) at cloud resolving scales. At observed lightning locations within individual grid columns, their nudging method imposed incremental increases of water vapor mass (q_v) toward saturation with respect to water within a confined layer and, thus, forced a local enhancement of thermal buoyancy (Houze 1993; Braun 2002; Fierro et al. 2012b). Over a large range of forecast days, F15 showed that this lightning nudging method improved the analysis and short-term forecast of accumulated precipitation, with the best improvements obtained for mesoscale outflow-dominated systems.

Prior assimilation efforts using variational methods within convection-allowing models have shown that assimilating other sources of data such as radar reflectivity or cloud information through pseudo-observed relative humidity (or q_v) also resulted in noteworthy improvements in the short-term forecasts of accumulated precipitation at parameterized-convection scales (>10 km; e.g., Marécal and Mahfouf 2002, 2003; Lopez and Bauer 2007) and convection-allowing scales (Caumont et al. 2010). No previous studies, however, have implemented assimilation of lightning data or a combination of lightning and radar data within a 3DVAR framework. The present study extends previous LDA techniques to incorporate lightning assimilation directly into a variational framework. To achieve this, an LDA method conceptually similar to that of Fierro and Reisner (2011) has been implemented within the three-dimensional variational data assimilation (3DVAR) system initially developed for the Advanced Regional Prediction System (ARPS) (Gao et al. 1999; Xue et al. 2001, 2003; Gao et al. 2004; Hu et al. 2006a,b; Stensrud and Gao 2010; Ge et al. 2010, 2012; Gao and Stensrud 2012; Gao et al. 2013).

A major motivation for this work is the imminent availability of GLM total lightning data over most of the

American hemisphere. This study makes use of lightning data detected by the ENTLN and the Oklahoma Lightning Mapping Array (OK-LMA; MacGorman et al. 2008). Because both the ENTLN and OK-LMA are able to detect a moderate to high fraction of the IC flashes in central Oklahoma (F12a; MacGorman et al. 2008), the density data derived from each of these networks are reasonable proxies for the total lightning densities expected to be delivered by the GLM. The assimilated lightning metric derived from ENTLN data will be referred to as the ENTLN source density (ESD) (similar to what was used by F12a) and the lightning metric derived from OK-LMA data as the flash extent density (FED). The present study evaluates the impact of assimilating either of these two-dimensional gridded total density rates in a 3DVAR framework within a convection-allowing model.

The case examined is the severe weather outbreak of 24–25 May 2011, which had a total of 12 tornado reports in central Oklahoma (cf. Fig. 1 of F12a; Kosiba et al. 2012; Wurman and Kosiba 2013; Tanamachi et al. 2015; Houser et al. 2015). Half of these tornadoes were rated [enhanced Fujita (EF) scale] EF-3 or greater, and two were rated EF-4 as they tracked dangerously close to the Oklahoma City metropolitan area. The reader is invited to consult F12a for more details on the synoptic situation of this day. The first rationale for selecting this case is the challenging nature of this forecast (F12a), which is reexamined here using different datasets for model initialization (described below in section 3). In particular, this work will highlight how the performance of the model is affected when either lightning and/or radar data (radial winds and reflectivity fields) are assimilated. The second rationale is the availability of three-dimensional lightning data from the OK-LMA over the area of interest (MacGorman et al. 2008). The lightning and radar data used for the assimilation and validation are briefly described in section 2. The setup of the model simulation and data assimilation procedures are introduced in section 3. The results are presented in section 4, followed by the conclusions in section 5.

2. Data used for assimilation and validation

The first source of lightning data for the present study is the ENTLN broadband (1–12 MHz) network, which as of 2011 consisted of about 150 ground-based sensors over the contiguous United States (CONUS). The ENTLN has a detection efficiency of about 40%–50% for ICs and over 95% for CGs over the study region in the western two-thirds of Oklahoma, with an accompanying location accuracy varying from tens of meters in dense areas of the network to about 200 m elsewhere (e.g., see Fig. 6 in F12a). Because, as noted in F12a, the ENTLN occasionally locates more than one pulse or source per flash, the ENTLN-derived data used for the assimilation in this work are referred to as source density rates instead of flash density rates.

The second source of lightning data is the OK-LMA very high-frequency network (Fig. 1), which is able to detect individual sources during the propagation of a lightning channel in three dimensions (Rison et al. 1999; Thomas et al. 2004; MacGorman et al. 2008). As of May 2011, the OK-LMA consisted of 11 stations in central Oklahoma (MacGorman et al. 2008; Griffin et al. 2014). Each sensor detects very high-frequency radio emissions from both IC and CG flashes. The system then uses the time-of-arrival method (six or more stations) to compute the location and time at which the sferics were produced by a developing lightning channel (Rison et al. 1999; Thomas et al. 2004; MacGorman et al. 2008). The OK-LMA location accuracy varies from tens of meters at the center of the network to about 500 m at a radius of about 100 km. Because of the limited number of OK-LMA stations, the total coverage of this network is limited relative to the national coverage of ENTLN. Over the study region, however, OK-LMA is able to detect the vast majority (i.e., ≥90%) of all the flashes (i.e., ICs + CGs) in three dimensions with a source location accuracy averaging 100 m. Because it maps the three-dimensional structure of individual flashes, it is possible to derive FEDs, which in contrast to ESDs, reflect the spatial extent of individual flashes. FED serves as a more accurate proxy for the data anticipated by GLM, which consist of FEDs derived from luminous pixel events that are grouped into individual lightning flashes at a resolution of approximately 8 km over CONUS (Goodman et al. 2013). Thus, emphasis will be placed on the assimilation of OK-LMA-derived FEDs.

The present 3DVAR code has capability to assimilate traditional observations as well as remote sensing data including three-dimensional radar reflectivity and radial velocity observations from the WSR-88D network. Following F12a and F14, the modeled reflectivity fields are evaluated against observed radar reflectivity fields from the three-dimensional National Mosaic and Multisensor Quantitative Precipitation Estimation product from NSSL (NMQ; Zhang et al. 2011), which were made available in 5-min increments back in 2011. The horizontal grid spacing of the NMQ dataset is 0.01° and the vertical grid spacing stretches from 250 m between $z = 500$ m and 3 km MSL, to 500 m between $z = 3$ and 9 km, and to 1 km above that until 18 km.

Last, the simulated accumulated precipitation fields were evaluated against the National Centers for Environmental Prediction's stage-IV multisensor hourly rainfall accumulation estimates (Baldwin and Mitchell

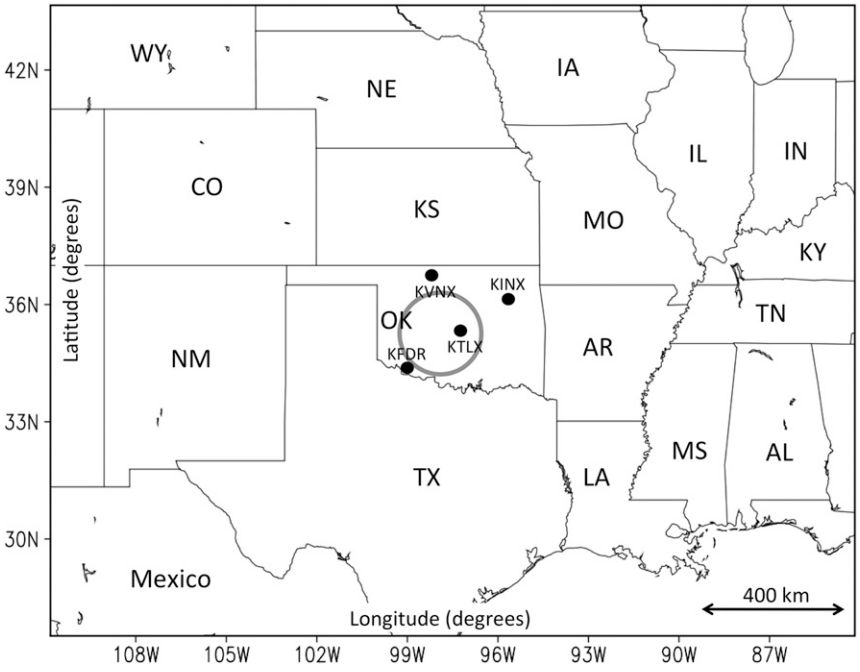

FIG. 1. Sketch of the simulation domain, D01 (3-km horizontal grid spacing) with the black dots denoting the locations of the WSR-88D sites used and tested in the ARPS 3DVAR code herein. The gray circle indicates the area where the lightning sources' location accuracy is ≤300 m for the stations composing the OK-LMA network as of May 2011. The U.S. states are indicated by their usual abbreviations.

1997) made publicly available by the Earth Observing Laboratory.[1] Despite being a dataset widely used to evaluate forecast performance, it does suffer from several limitations including radars being out of calibration, rain gauges being clogged, and partial beam blockages due to buildings and terrain. To compare model and observations, the hourly stage-IV data were remapped from its native 4-km polar stereographic grid onto the 3-km Mercator grid of the simulation domain (Fig. 1).

3. Simulations setup

a. Model grid and physics configuration

The forecast model used in this study is the three-dimensional compressible nonhydrostatic WRF Model (version 3.6.1) with Advanced Research WRF dynamic solver (WRF-ARW; Skamarock and Klemp 2008). Following the philosophy of F14 and F15, the overall physics and grid configuration are similar to that of the experimental real-time CONUS convection-allowing model forecasts conducted by the National Severe Storms Laboratory (NSSL-WRF; Kain et al. 2010). The main differences between the current setup and that of NSSL-WRF are the use of a 3-km grid in lieu of 4 km and the smaller size of the simulation domain.

In this study, the simulations are conducted on one single domain with a uniform horizontal grid spacing of 3 km and horizontal dimensions in grid points of 801 × 601 (Fig. 1). The stretched vertical grid has 35 levels with its top at 100 hPa (~15.5 km) and the computational time step is 15 s. The dataset utilized to derive initial and time-dependent lateral boundary conditions employs the hourly, 13-km Rapid Update Cycle (RUC; Benjamin et al. 2004, now known as the Rapid Refresh or RAP since 2012) analysis at 2000 UTC 24 May 2011 and subsequent forecast data for a 4-h period. The simulations are terminated at 0000 UTC 25 May, because this study focuses chiefly on the analysis and 1–3-h forecast of the tornadic cells that formed in the western two-thirds of Oklahoma and does not consider later times when these individual supercells merged into a quasi-linear convective system (F12a). Further motivations for not focusing on later forecast times are that (i) the performance of convection-allowing data assimilation methods is usually confined to the first 4–8 h of the forecast owing to error growth in the large-scale environment progressively saturating the model solution (e.g., F15 and studies cited within) and (ii) the overall poor quality of the lightning data from the OK-LMA at longer ranges outside the body of Oklahoma.

[1] See http://data.eol.ucar.edu.

The use of RUC data as convection develops in the observations is intentional to demonstrate that both LDA and radar data assimilation can force the initiation of observed convection. Although there is no model spinup prior to performing the data assimilation (DA), starting the DA when convection is developing in the target area in the observations also facilitates the qualitative and quantitative analysis of the impacts of the respective DA procedures.

It is also relevant to mention that the model top in our simulation could not exceed 100 hPa because the RUC files employed herein do not contain data above that level. Although this is admittedly too shallow to accurately resolve the vertical extent of deep moist convection, the results show that this dataset is still adequate to address the salient goal of this study raised in (ii) above. One additional limitation of this RUC dataset is the absence of 2D soil arrays required to activate the surface layer parameterization in WRF. Because, however, these simulations were initialized near the peak hours of solar heating (i.e., 2000 UTC), sensitivity tests (not shown) employing another data source that includes the 2D soil arrays (i.e., 12-km North American Mesoscale Forecast System dataset), revealed insignificant differences in the evolution of the forecast convection and surface variables such as temperature and moisture.

As in NSSL-WRF, the simulations employ the single-moment 6-class bulk microphysical scheme (WSM6) of Hong and Lim (2006). The six bulk species are rain, cloud water, cloud ice, snow, graupel, and hail. The boundary layer is parameterized following the 1.5-order closure Mellor and Yamada (1982) turbulence kinetic energy scheme adapted by Janjić (1994) with Monin–Obukhov–Janjić similarity theory for the subgrid-scale turbulence processes (Chen et al. 1997). Atmospheric radiation is parameterized following Dudhia (1989) for the shortwave and the Rapid Radiative Transfer Model (RRTM) for the longwave (Mlawer et al. 1997).

b. *Data assimilation procedures*

1) RADAR

The assimilation of radar data in the present study always includes both radial velocity and reflectivity information. In F14, the storm-scale 3DVAR system could only be directly used with the ARPS model. To use this 3DVAR package with WRF, F14 made use of two separate executables that interpolated the 3DVAR analysis variables back and forth between the WRF and ARPS model grids. In this study, however, a direct interface for the WRF Model has been developed (Zhuang et al. 2016), which obviates the need to interpolate the 3DVAR analyses back and forth. The data from each radar are quality controlled (e.g., dealiasing radial velocity, removing nonmeteorological scatterers) and interpolated onto the WRF grid (for thinning purpose) before the DA. When reflectivity data from multiple radars overlap at a given grid point, the largest value is chosen. For each 3DVAR analysis, two passes are used in the analysis with horizontal (vertical) decorrelation length scales for all control variables set to 24 (12) km, respectively. Using an additional pass for the 3DVAR with smaller decorrelation length scales is designed to extract more convective-scale information from radar data. The background error variances for the model variables are derived from statistics of RUC 3-h forecasts over several years and the background error correlations are modeled by a recursive filter (Purser et al. 2003a,b). The radial velocity data are used in the 3DVAR analysis to adjust the three Cartesian components of the wind field. Both potential temperature θ and pressure (not only surface pressure) are part of the control variables, and these fields can also be changed if other types of observations such as Mesonet data were also assimilated. There is no cross correlation between wind field, θ, and pressure. More detail of this version of 3DVAR with WRF interface can be found in Zhuang et al. (2016). Radar reflectivity measurements are used in the cloud analysis to adjust the hydrometeor variables (i.e., cloud water, cloud ice, rain, snow, and graupel/hail mixing ratios) and θ (Albers et al. 1996; Zhang et al. 1998; Brewster 2002; Hu et al. 2006a,b) following the 3DVAR analysis. As mentioned in section 3b(2) below, pseudo-observations for q_v are derived from the lightning density rates rather than being provided by the cloud analysis. The cloud analysis has an option to generate pseudo-q_v observations for (high) relative humidity based on radar data, which have not been activated in the base experiments to better dissociate/isolate the impact of the LDA (Table 1). To gauge the impact of radar-derived pseudo-q_v observations, however, two additional experiments were performed with the latter option activated (Table 1).

The use of a cloud analysis to adjust hydrometeor variables and a 3DVAR analysis to adjust the kinematic state with radial velocities was intentional to mirror an arguably more standard setup. Given a radar DA setup using all the available data provided by the radars and despite the lower density information contained in 2D lightning datasets relative to volumetric radar scans, the LDA still is able to force convection near the observed locations. To better underscore the effectiveness of the assimilation procedures, all the experiments in this study employ only one 3DVAR analysis (namely at 2000 UTC).

As highlighted in section 2, the 3DVAR analysis in the present study assimilates WSR-88D level-II data

TABLE 1. The left column lists the nomenclature/abbreviations used for all the simulations/experiments analyzed in this study. The second column from the left briefly describes the type of experiments. The second column from the right indicates the type of data that were assimilated with "dBZ" standing for radar reflectivity and "Vr" for radial velocity. The right column shows which model variable(s) is (are) impacted by the respective assimilation experiments with the symbols used to identify those variables bearing their usual meaning. For convenience, the experiments are listed in the order they appear in the text (as in Fig. 3).

Experiment	Description	Data assimilated	Model variables impacted
CTRL	Control run	None	None
OKLMA	Lightning assimilation run.	OK-LMA flash extent density rates	q_v (LCL-15 km)
RAD	Radar data assimilation run	Vr and dBZ	q_r, q_g, q_i, q_s, q_h, u, v, w, θ
RAD + OKLMA	Lightning + radar assimilation run	OK-LMA flash extent density rates, Vr, and dBZ	q_v (LCL-15 km), q_r, q_g, q_i, q_s, q_h, u, v, w, θ
ENTLN	Lightning assimilation run	ENTLN source density rates	q_v (LCL-15 km)
RAD-noVR	Radar data assimilation run without Vr	dBZ	q_r, q_g, q_i, q_s, q_h, θ
RAD-noVR + OKLMA	Radar data assimilation run without Vr	OK-LMA flash extent density rates and dBZ	q_v (LCL-15 km), q_r, q_g, q_i, q_s, q_h, θ
RAD-noCLDAN	Radar data assimilation run without the cloud analysis	Vr	u, v, and w
RADQV	As in RAD but with q_v adjustments by the cloud analysis	Vr and dBZ	q_v, q_r, q_g, q_i, q_s, q_h, u, v, w, θ
RAD45dBZ	RAD experiment mimicking the LDA procedure for OKLMA (see text)	Vr and dBZ	q_v, q_r, q_g, q_i, q_s, q_h, u, v, w, θ
OKLMA ztop5km	Lightning assimilation run	OK-LMA flash extent density rates	q_v (LCL-5 km)

obtained from the National Centers for Environmental Information[2] (e.g., F14). Radar reflectivity and radial velocity data have been utilized from KTLX (Oklahoma City, Oklahoma), KFDR (Frederick, Oklahoma), KVNX (Vance Air Force Base, Oklahoma), and KINX (Tulsa, Oklahoma)(Fig. 1). These four sites provide a reasonable coverage of the storms during the target period of analysis, particularly above ~3 km MSL where the scan volumes overlap (Zhang et al. 2011; Gao et al. 2013). For this reason, radar reflectivity fields in the observations and simulations are shown at 4 km MSL. Observed reflectivity values are thresholded at 20 dBZ for altitudes below 1.5 km MSL and at 15 dBZ at higher altitudes in order to reduce unwanted influence of weak radar returns or nonmeteorological scatterers.

2) LIGHTNING

To assimilate lightning data within the ARPS 3DVAR package described in section 3b(1), the raw data originating from ENTLN and OK-LMA are respectively converted into gridded density rates (per 3-km grid cell herein). Given the latitude and longitude points of the WRF grid, the conversion of the ENTLN source data (given in the format of "time, latitude, longitude") into two-dimensional ESD rates (per 10 min herein) is relatively straightforward. The conversion of the three-dimensional very high frequency (VHF) sources of the OK-LMA into two-dimensional FED rates, however, first requires spatial and temporal assumptions to group source points into individual flashes. Following Lund et al. (2009), the VHF lightning data are grouped into individual flashes using criteria based on the distance (500 m) and time (250 ms) of each mapped VHF events from previous VHF events (MacGorman et al. 2008). Only flashes containing more than 10 VHF sources are used in the assimilation experiments. It is relevant to highlight that when flash rates are as large as those produced by the supercells on 24 May, the estimate of flash rate using this algorithm can be sensitive to relatively modest changes in the aforementioned spatiotemporal thresholds. Thus, the LMA-derived flash rates should be considered as approximate (MacGorman et al. 2008). The flashes are then binned into 10-min intervals on the 3-km model grid (Fig. 1) to yield the final FED product. A flash is counted once within a given grid cell or pixel if any portion of the lightning flash entered the area.

[2] See http://www.ncdc.noaa.gov/oa/radar/radardata.html.

As mentioned in the introduction, the LDA procedure implemented in the 3DVAR code follows the same philosophy as in Fierro and Reisner (2011) and F12a. At observed lightning locations (i.e., grid columns), the LDA sets its pseudo-observation q_v to its saturation value over water ($q_{v\text{sat}}$) in the layer between the lifted condensation level (LCL, a surrogate for cloud base) and an assumed fixed height of 15 km. Using a fixed height, however, does not take into account seasonal or geographical variations. Because relative humidity is proportional to the ratio between q_v and $q_{v\text{sat}}$, creating pseudo-observed fields whereby the relative humidity = 100% or $q_v = q_{v\text{sat}}$ at observed lightning locations is equivalent. For simplicity, the q_v increase herein is not made proportional to the observed gridded density rate or inversely proportional to the simulated graupel mixing ratio at that grid point as in F12a, but instead follows the simpler methodology of Fierro and Reisner (2011). Because low values of FED and ESD within deep convective storms often are associated with lightning channels extending into their horizontally extensive anvil clouds (e.g., Fig. 2; Weiss et al. 2012), a lower cutoff value of 50 FED and 10 ESD [$(10\,\text{min})^{-1}$] is set to avoid promoting the formation of unrealistically wide updrafts. In other words, observed density rates lower than the cutoff threshold simply are interpreted as nonupdraft areas by the LDA and, hence, the pseudo-q_v observations are not created. A future implementation could have an adjustable cutoff threshold to allow an impact on low flash rate storms or to capture the early stages of potentially severe storms (when density rates are still low).

After the density rates (i.e., 10-min FED or ESD) have been computed, the next procedure converts these into three-dimensional q_v pseudo-observations via the following procedure: Wherever the density rate is below the threshold, the pseudo-q_v in the corresponding grid column is not created, whereas at observed lightning locations meeting or exceeding the aforementioned thresholds, pseudo-q_v is set to its corresponding saturation value with respect to water between the LCL and a fixed upper height. For each grid point within this prescribed layer, the pseudo-q_v (i.e., $q_{v\text{sat}}$) is computed using the model background temperature and pressure at that grid point. Then, these pseudo-q_v observations are assimilated through the 3DVAR analysis by minimization of the so-called cost function, which includes the background term and observation term for q_v. The observation error for q_v was set to $3 \times 10^{-3}\,\text{kg kg}^{-1}$ and the background error for q_v is set to $10^{-2}\,\text{kg kg}^{-1}$. As mentioned in section 3b(1), the horizontal (vertical) decorrelation length scales for all control variables, including q_v, are set to 24 and 12 km, respectively.

In contrast to Fierro and Reisner (2011) and F12a, where lightning data were continuously assimilated over a given period (e.g., 2 h in F12a), the lightning data in all the experiments in this study only are assimilated at one single time (i.e., 2000 UTC). In other words, while the incremental increase in q_v in F12a is maintained at each computational time step throughout each 10-min interval within a 2-h period, the q_v increase in the present study is applied only once. The assimilation and model initialization time of 2000 UTC was selected because the lightning observations are associated with the development of the tornadic supercell thunderstorms in northwest Oklahoma (F12a). The 10-min ESD or FED rate fields that are assimilated at 2000 UTC are shown in Figs. 2a and 2c, respectively. The LDA includes the densities accumulated for the 10-min period prior the assimilation time (i.e., between 1950 and 2000 UTC for the 3DVAR initialization).

4. Results

In this section, the performance of the 3DVAR assimilation of FED data from the OK-LMA (denoted OKLMA), radar data (RAD), or combined (RAD + OKLMA) first are evaluated against the observations and against a control run (CTRL) that assimilated no data. An additional 3DVAR experiment assimilating ENTLN-derived source density data also is shown for comparison. All the experiments presented in this study are listed in Table 1. For all the simulations herein, this analysis focuses on the tornadic supercells that developed in northwest Oklahoma (cf. Fig. 1 in F12a) and does not place emphasis on the observed remote convection that occurred beyond the range of the OK-LMA (Figs. 1 and 2).

During the first hour of simulation at 2100 UTC, CTRL exhibits weak and localized radar echoes in northwest Oklahoma (cf. Figs. 3a,b; 4a,b; and 4d,e), owing to poor resolution of boundary layer processes that force convection initiation in F12a and also because of the longer time required for modeled storms to develop without assimilation. At 2100 UTC, those weak radar echoes in CTRL are associated with only weak ($<8\,\text{m s}^{-1}$) midlevel (4 km) vertical velocities and no appreciable vertical vorticity (i.e., $<10^{-3}\,\text{s}^{-1}$, Fig. 3b). By about 2 h 30 min in the forecast (i.e., 2230 UTC), however, CTRL is able to reproduce some of the observed storms in central and south-central Oklahoma while missing other storms farther south near the Oklahoma–Texas border (not shown).

Assimilating only the FED derived from OK-LMA data noticeably improved the representation of the convection, as evidenced by the presence of supercell-storm objects in northwest Oklahoma at 2100 UTC (arrows in Figs. 3a–c). Since the introduction of water vapor mass at observed lightning locations helps accelerate the development of convection, the evolution

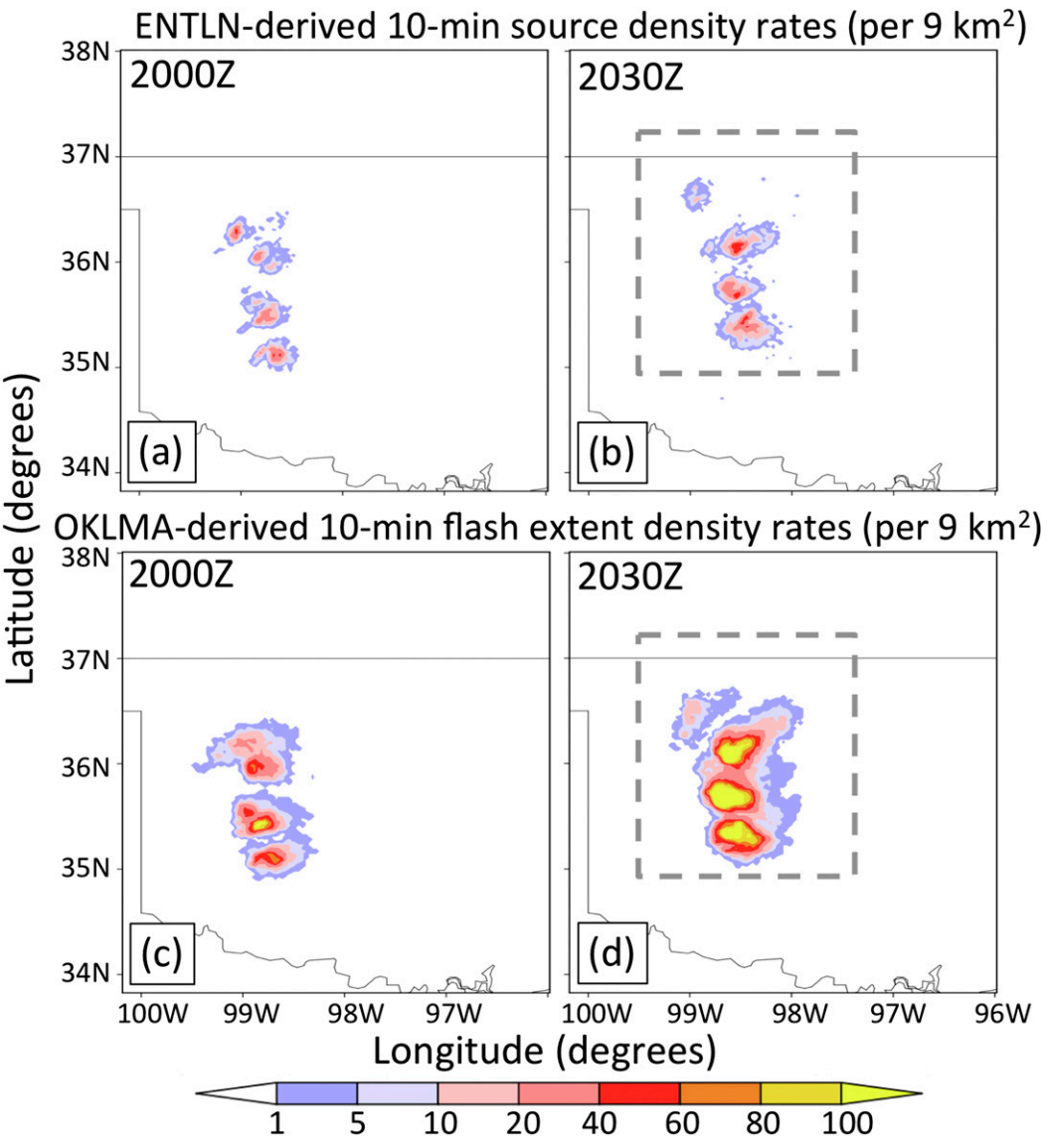

FIG. 2. (a),(b) ENTLN-derived 10-min source densities $[(9\,\text{km}^2)^{-1}]$ up to the indicated time, where 2000 UTC corresponds to the analysis time in the base experiments. (c),(d) As in (a),(b), but for the OK-LMA-derived 10-min flash extent densities $[(9\,\text{km}^2)^{-1}]$. Because of the limited detection range of OK-LMA, the observations mainly are confined to the state of Oklahoma at those times. To facilitate comparison, both lightning metrics use the same color scale shown at the bottom. By design, (a) and (c) show the lightning data that are assimilated. To focus on the tornadic storms impacting the Oklahoma City metro area, the individual panels also depict the geographical area of the analysis domain used throughout the analysis. The zoomed analysis domain is centered over the tornadic supercells that formed in northwest Oklahoma between 1930 and 2000 UTC. The dashed gray box in (b) and (d) highlights the boundaries of the subdomain of Fig. 3.

of the observed storms in north-central Oklahoma is better depicted throughout the first 1 h 30 min of the forecast (arrows in Figs. 5a–f). Note that despite this improvement, the 1-h forecast still misses some storms in west-central Oklahoma. In the OKLMA experiment, most of the storms that were promoted by the assimilation in northwest Oklahoma appear to exhibit classic radar-observable supercellular traits such as an elongated "V shape" and hook echo appendage (arrows in Figs. 5e,f) associated with pronounced, collocated low-level vertical vorticity and updraft cores (arrows in Fig. 3c). The experiment assimilating only the ENTLN-derived source densities revealed forecast improvements that were similar overall to those in OKLMA (cf. Figs. 3c,f).

When radar data (i.e., radial winds and reflectivity, Table 1) are assimilated, the improvements in the

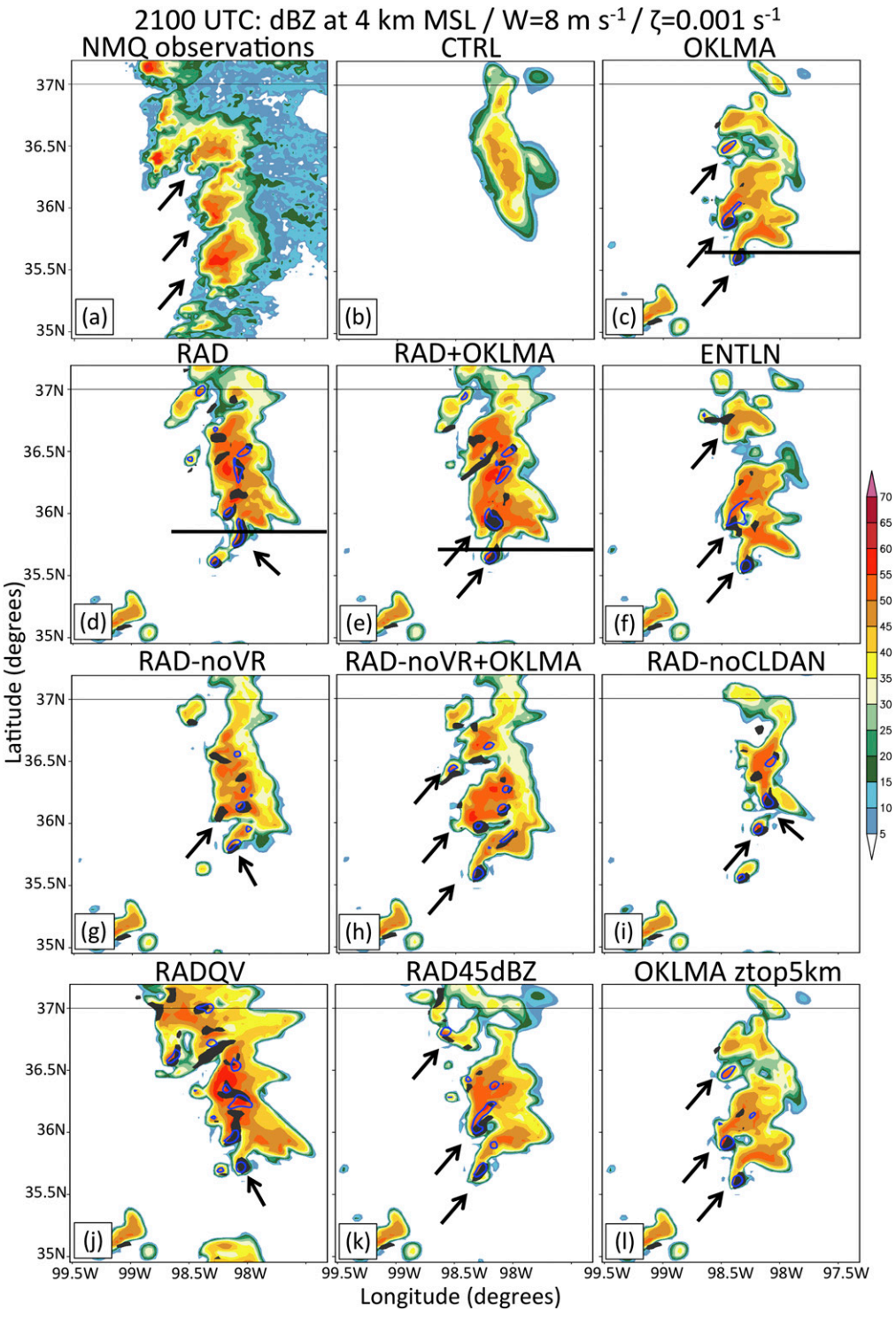

FIG. 3. Horizontal cross sections at 2100 UTC (1-h forecast) over the subdomain highlighted in Figs. 2b and 2d of radar reflectivity (dBZ) at $z = 4$ km MSL overlain with the 8 m s^{-1} vertical velocities (blue contour) and vertical vorticities of 10^{-3} s^{-1} (solid black) for (a) the NMQ observations and (b)–(l) all the experiments listed and described in Table 1. For convenience, the experiments in (b)–(l) are listed in the order they appear in the text, which is the same as in Table 1. Black arrows highlight the convective elements specifically discussed in the text and the horizontal black line shows the respective locations of the vertical cross sections shown in Fig. 6. As can be seen in this figure, the location of the vertical cross sections was purposively chosen to be slightly north of the main updraft of one particular cell to simultaneously capture a portion of its anvil and convective core. This convective cell was selected because all DA runs were able to reproduce it.

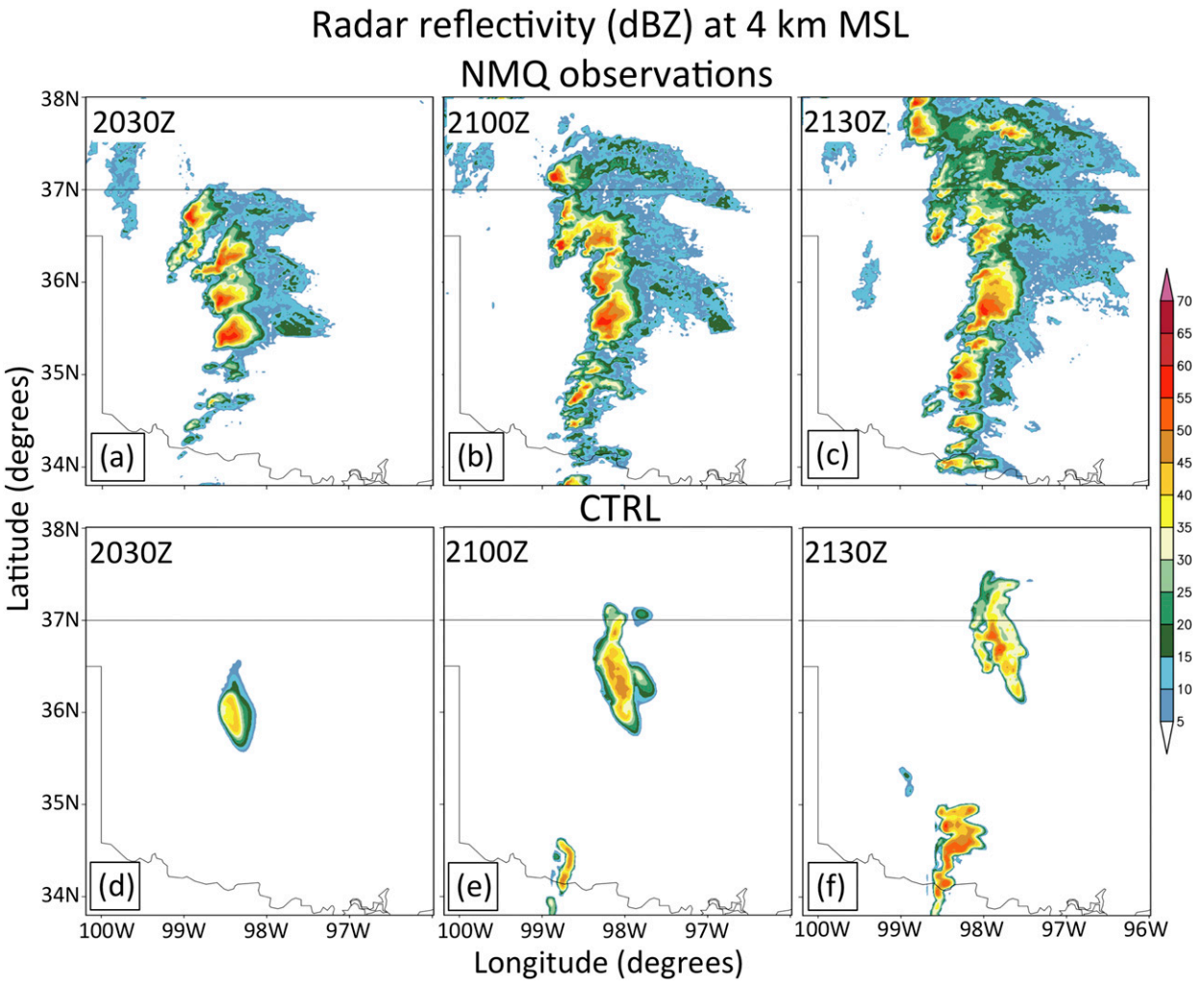

FIG. 4. Horizontal cross sections of radar reflectivity at 4 km MSL from the 1-km resolution, 3D NMQ product interpolated onto the local 3-km D01 domain at (a) 2030, (b) 2100, and (c) 2130 UTC 24 May 2011. (d)–(f) As in (a)–(c), but for the simulated reflectivities in CTRL. By design of the assimilation procedure, 2030, 2100, and 2130 UTC correspond here to the 30-min; 1-h; and 1-h 30-min forecasts, respectively. Legends for color and shadings are shown on the right.

representation of the convection at the 1-h forecast over CTRL are overall similar, but differ from those in OKLMA. At the 1-h forecast, RAD reveals a more solid line of storms compared to fairly discrete cells for OKLMA (cf. arrows in Figs. 3c,d) and for the observations (Fig. 3a). The similarity between the forecasted and observed morphologies of radar echoes in this line of storms arguably worsens later in the forecast period (e.g., Fig. 5i). As might be expected, these differences are also reflected in the number and distribution of updrafts; OKLMA produces three distinct updrafts in northwest Oklahoma in the 30-min (not shown) and 1-h forecasts (cf. arrows in Fig. 3c), while RAD produces more than twice as many updrafts, with only the southernmost storm exhibiting noticeable supercellular characteristics (cf. arrows in Figs. 3d and 5h). At the 30-min and 1-h forecasts, both OKLMA and RAD miss some of the observed storms in central OK (cf. Figs. 5b,c; 5e,f; and 5h,i).

When both the OKLMA-derived FED rates and radar data are assimilated, the representation of the convection at the 30-min forecast (2030 UTC) is further improved over assimilating each type of data separately in RAD and OKLMA as the horizontal reflectivity structures are simultaneously more isolated and more consistent with the mature supercell structures in the observation (arrows in Figs. 4d and 5a,d,g,j). This improvement occurred because the storms in RAD + OKLMA benefited from both the earlier development of the hydrometeor fields through the cloud analysis in RAD and the more targeted updraft forcing of the LDA. Although RAD + OKLMA produces overall the best 30-min forecast, the reflectivity fields

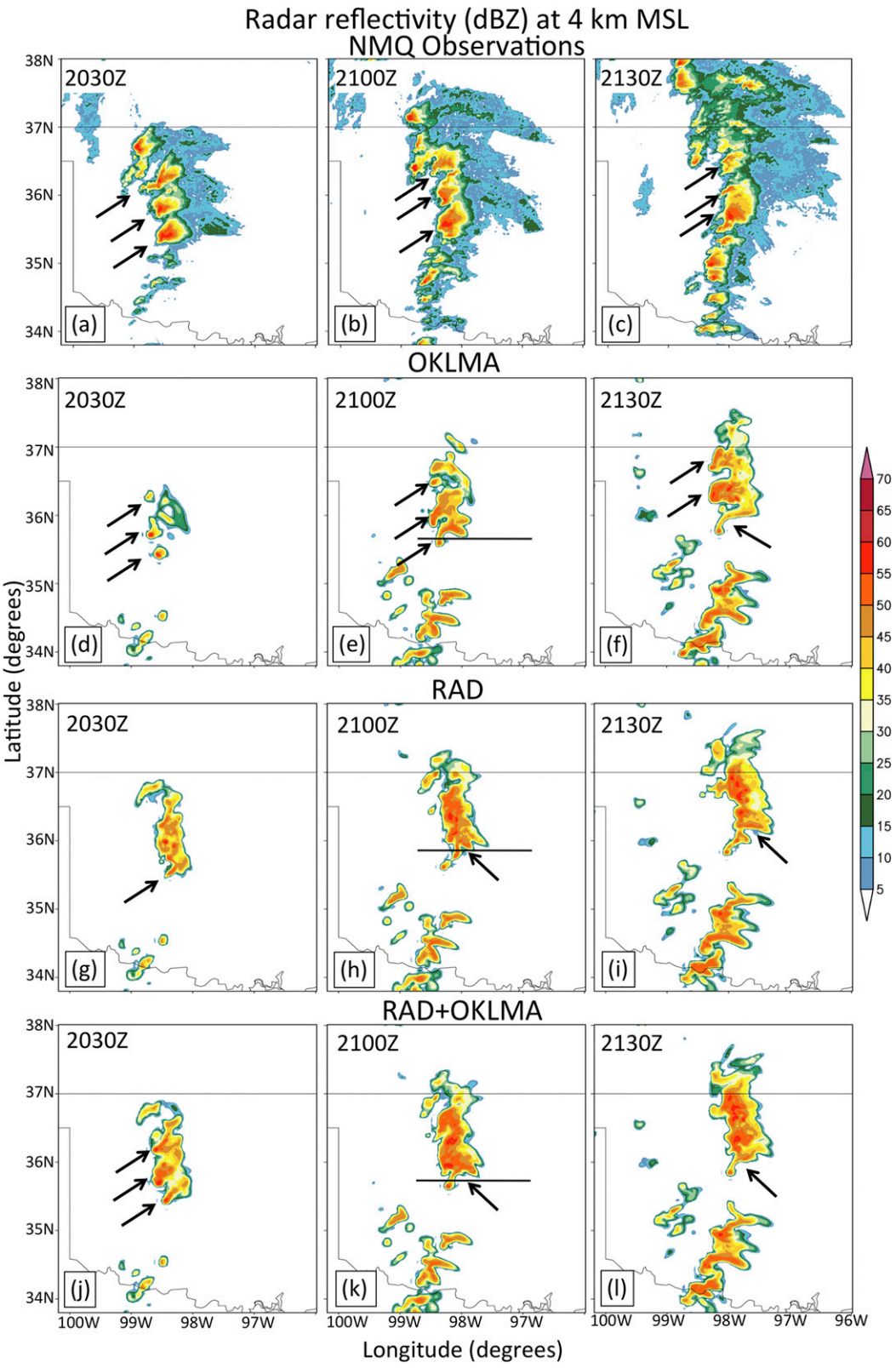

FIG. 5. As in Fig. 4, but for the main 3DVAR assimilation experiments with the NMQ observations shown again for reference in (a)–(c). The short-term forecasts for OKLMA, RAD, and RAD+OKLMA are shown in (d)–(f), (g)–(i), and (j)–(l), respectively. The 30-min (2030 UTC), 1-h (2100 UTC), and 1-h 30-min (2130 UTC) forecasts are shown from left to right. As in Fig. 3, black arrows highlight the convective elements specifically discussed in the text and the horizontal black line shows the respective locations of the vertical cross sections shown in Fig. 6.

and the main updrafts of these supercells start merging too early (Figs. 5b,c,k,l), which is partly associated with the earlier development of the hydrometeor fields in RAD (Figs. 5a,d,g,j). Confirmed by a suite of additional experiments below, one additional factor for this earlier reflectivity merger in RAD is that the DA-induced forcing is applied over a relatively broad grid volume compared to OKLMA.

Figures 3g–l show additional sensitivity tests that highlight some important aspects of the lightning and radar data assimilation procedures. When the radial velocity fields were not assimilated in the 3DVAR analysis (with the cloud analysis activated: RAD-noVR), the storms are overall weaker compared to RAD (cf. Figs. 3d and 3g). This is because radial velocity assimilation was shown to help improve the intensity of updraft and rotation (e.g., Gao et al. 2013). When the OKLMA data also were assimilated in RAD-noVR, similar relative forecast improvements between RAD and RAD + OKLMA were obtained (cf. Figs. 3d,e and 3g,h). If the cloud analysis is not activated, the forecast is degraded owing to a delay in the initiation and development of the observed storms (Figs. 3d,i). Allowing the cloud analysis to adjust the q_v field or the relative humidity field based on the observed reflectivities (RADQV; Fig. 3j) resulted in the largest number of secondary updrafts and in even more disorganized convection compared to RAD (Fig. 3d) and, thus, compared to the observations (Fig. 3a). As confirmed by an additional experiment described below (RAD45dBZ in Fig. 3k), this was partially traced back to the use of a relatively small reflectivity threshold (~15 dBZ), which caused the induced thermal (q_v) forcing by the cloud analysis to be applied over a relatively broad grid volume.

Consistent with this, the RAD-based experiment in Fig. 3k demonstrates that it is feasible to mimic the convective response (and forecasts) from the LDA experiments by modifying specific key input parameters in the 3DVAR and cloud analysis to confine and enhance thermodynamic forcing near convective cores (RAD45dBZ). The following procedure was devised to achieve this: (i) restrict the kinematic forcing to areas with reflectivity values ≥45 dBZ (instead of ≥15 dBZ), (ii) set the horizontal decorrelation (influence) radius to 1–2 grid points (i.e., 3–6 km) instead of 4–8 grid points (12–24 km), (iii) set the vertical influence distance to 1–2 grid points (instead of 4); and (iv) allow the cloud analysis to adjust q_v based on reflectivity observations to promote thermodynamic forcing.

Last, because the pseudo-q_v observations in the LDA experiments are imposed over nearly the entire depth of the domain (i.e., up to z = 15 km), it is relevant to examine how the short-term forecast would be impacted if the pseudo-q_v observations in the LDA were restricted to lower levels (here, up to z = 5 km). The results ("OKLMA ztop5km" in Fig. 3l) revealed nearly identical 1-h forecast outcome compared to the base OKLMA experiment (Fig. 3c). This is consistent with the bulk of the water vapor mass in the atmosphere being confined at lower levels.

In other words, the results in Fig. 3 indicate that the differences in forecast behaviors between the LDA and the radar data assimilation runs are directly attributable to differences in the nature of the forcing mechanism(s) between the assimilation procedures. The LDA induces thermodynamic forcing in localized areas (Figs. 6b,d) while this radar data assimilation procedure promotes a combination of kinematic (three components of the wind field) and thermodynamic (changes in θ) forcing (Fig. 6c), over a relatively broader area followed by the direct insertion of hydrometeors through the cloud analysis. As a consequence, downdrafts in the radar data assimilation runs develop more quickly through sedimentation of precipitation while, in the LDA, locally strong updrafts must first develop before precipitation is produced in the model (Figs. 6e–h). The radar data assimilation affects mainly areas of reflectivities ≥15 dBZ while the LDA is applied only where the 10-min FED/ESD rates exceed a prescribed threshold (small area in Fig. 2). Thus, consistent with the results of RAD45dBZ (Fig. 3k), the thermal forcing (via θ adjustments) that ultimately promotes convection in RAD is imposed over a relatively broader grid volume than in the LDA runs. This explains why when the LDA is performed in tandem with RAD, locally strong supercell updrafts (Figs. 6d,h) are produced more readily and more quickly, thereby yielding to more realistic supercellular storm structures early in the forecast (Figs. 3c–e).

Because RAD does not directly adjust q_v during the assimilation, it is anticipated that the layer-averaged q_v between CTRL and RAD be identical. A closer inspection reveals, however, slight differences in layer-averaged q_v between CTRL (Fig. 6a) and RAD (Fig. 6c). This is because in RAD, q_v must be still slightly adjusted to accommodate the changes in the perturbation θ field.

As indicated earlier in this section, at 2100 UTC (1-h forecast) all DA runs are able to reproduce at least one distinct convective element with radar-observable supercellular traits consistent with the NMQ observations (see arrows in Fig. 3). To provide a more complete view of the structure of this cell, vertical cross sections through a portion of the convective core and the anvil (locations relative to the main updraft of this cell shown in Figs. 3c–e) are shown in Figs. 6i–k. Overall, all three cells reveal qualitatively similar reflectivity structures with one single dominant updraft extending up to the tropopause and with an anvil structure reminiscent of the weak echo overhang. As alluded to earlier, because the RUC data used herein have a model top set at 100 hPa

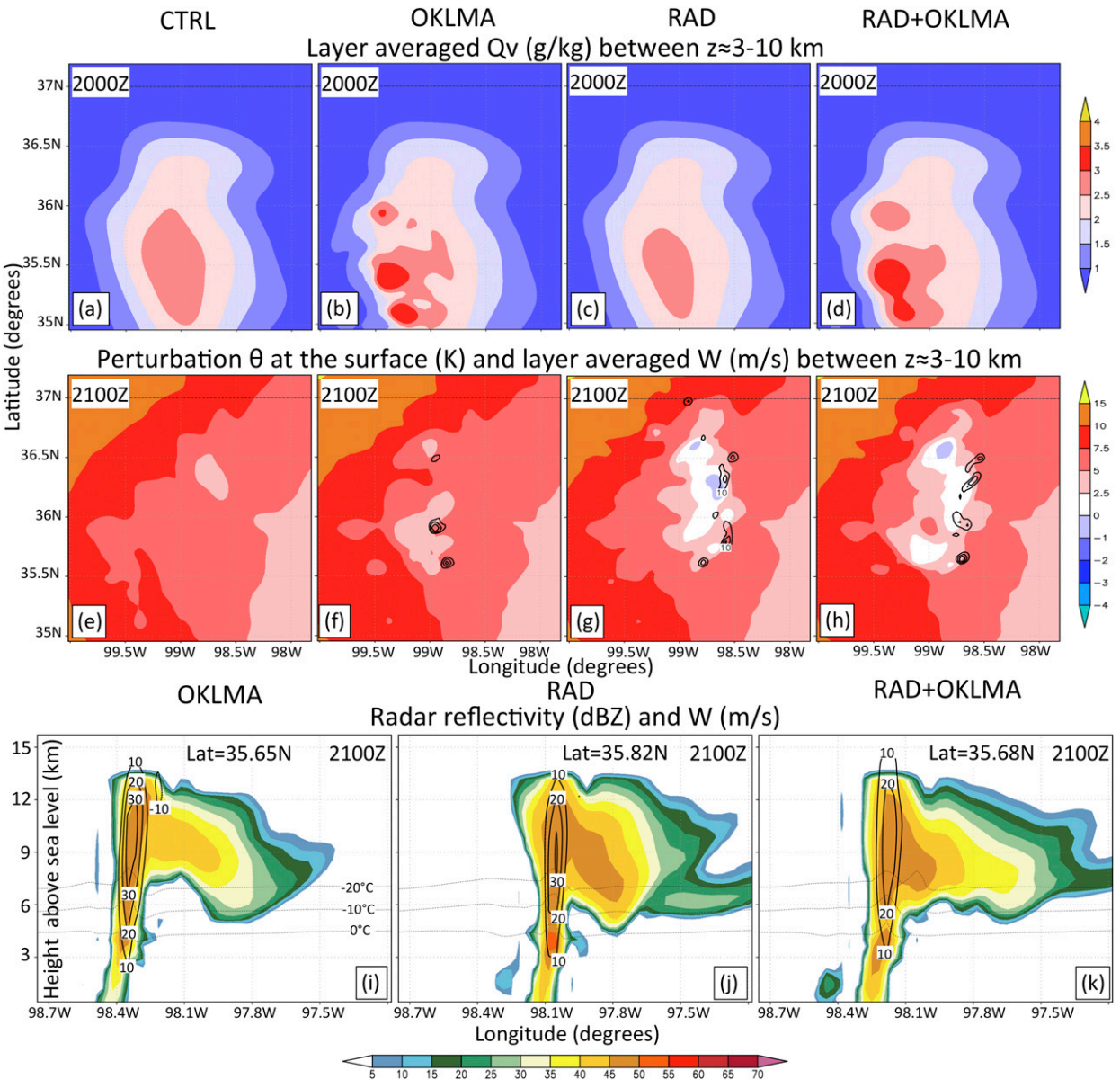

FIG. 6. (a)–(d) As in Fig. 3, but for the layer-averaged water vapor mass q_v between $z \approx 3$ and 10 km MSL at 2000 UTC. (e)–(h) As in (a)–(d), but for the surface perturbation potential temperature at 2100 UTC overlaid with the layer-averaged vertical velocities (black contours in 10 m s^{-1} increments) between $z \approx 3$ and 10 km MSL. Results are shown from (a),(e) CTRL; (b),(f) OKLMA; (c),(g) RAD; and (d),(h) RAD + OKLMA. Respective legends for the color shadings for the first two rows are shown on the right. (i)–(k) Vertical cross sections of radar reflectivity fields and vertical velocities (black contours in 10 m s^{-1} increments) at the locations denoted by the black horizontal lines in Figs. 3 and 5 for (i) OKLMA, (j) RAD, and (k) RAD + OKLMA.

(~15.5 km), the tropopause and simulated cloud tops are shallower (~13.5 km) than would be expected for strong supercells. While a model top of ~20 km (50 hPa) would have been more appropriate to properly resolve the vertical extent of deep moist convection, the RUC data used to initiate the model environment at the time when the incipient storms are starting to develop are sufficient to demonstrate that both the LDA and radar DA can force the initiation of observed convection.

Informed by these results, it is of interest to determine if the supercell radar characteristics seen in some of the simulated cells are consistent with improvements in tornadic potential. The tornadic potential of the observed and simulated storms is inferred by examining and comparing the tracks of the radar-derived 3–6-km maximum azimuthal shear associated with the observed mesocirculations (Fig. 7a) and the maximum updraft helicity in the model (Figs. 7b–f). Since the dominant midlevel

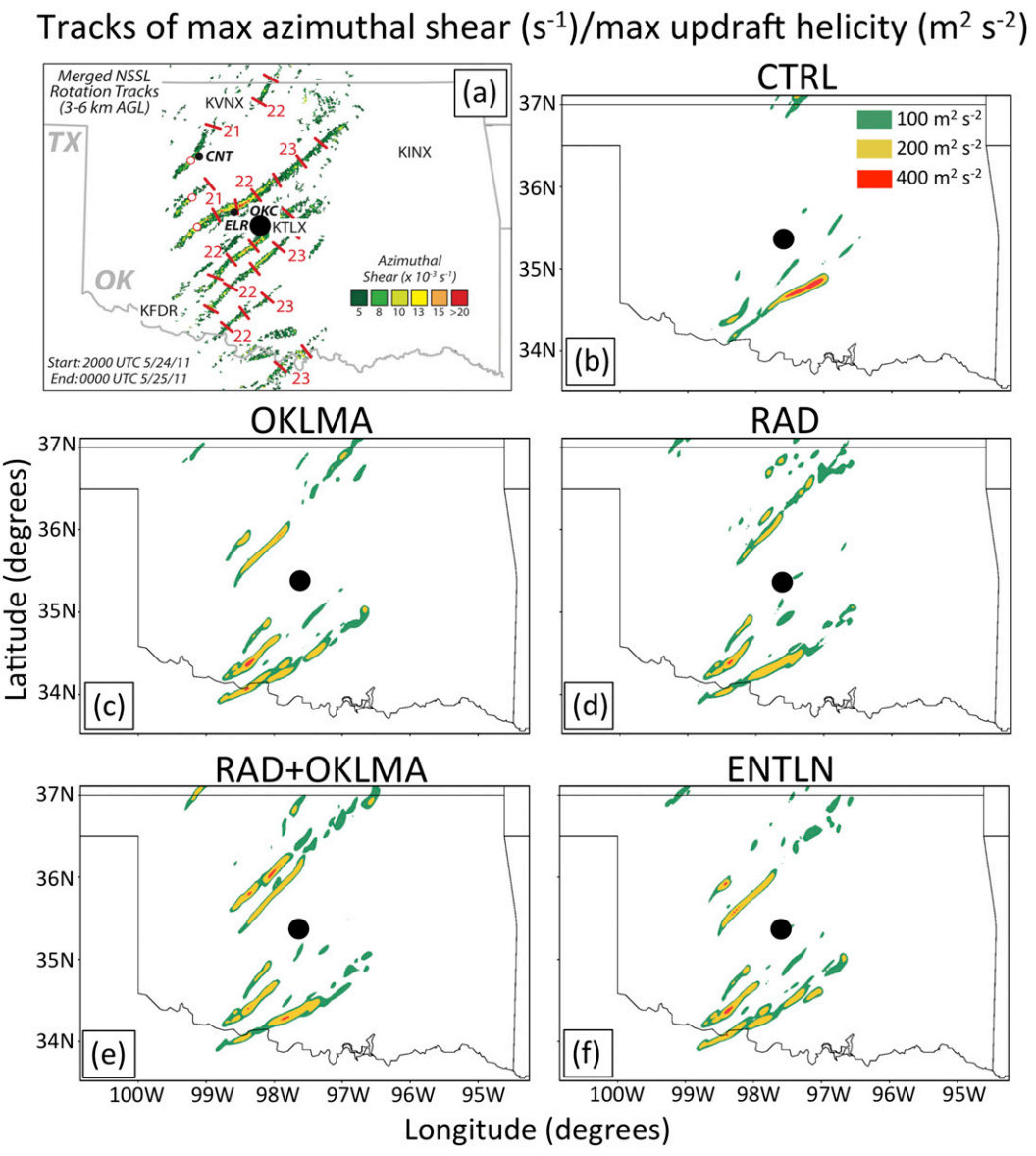

FIG. 7. Paths of significant midlevel mesoscale rotations in storms on 24–25 May 2011. The merged rotation tracks, which are depicted by the local maximum azimuthal shear ($\times 10^{-3}$ s^{-1}) in (a), were generated by B. Smith (NSSL) using data from all regional radars including KVNX, KINX, KTLX, and KFDR via NSSL's WDSS-II package (Smith and Elmore 2004; Lakshmanan et al. 2007; Smith et al. 2016). (b)–(f) As in (a), but for the simulated maximum updraft helicity tracks (m^2 s^{-2}) for (b) CTRL, (c) OKLMA, (d) RAD, (e) RAD+OKLMA, and (f) ENTLN experiments. The large black dot denotes the location of Oklahoma City. The location of the tornadoes near El Reno (ELR; Houser et al. 2015), and Canton (CNT; Kosiba et al. 2012) and half-hourly isochrones of observed mesocirculation positions are also displayed in (a). The overall time period of the tracks in all panels are shown for the duration of the simulation (2000 UTC 24 May–0000 UTC 25 May 2011). Color-fill legends are shown in (a) for the observations and in (b) for the simulations.

mesocirculation would be expected to interact with the main updraft of each observed storm to produce a local updraft helicity maximum, the observed azimuthal shear tracks may be qualitatively compared to the modeled updraft helicity tracks. Note that only the storms in northwest Oklahoma are active at the time of the 3DVAR initialization (i.e., 2000 UTC). The simulated helicity tracks $\geq$100 m^2 s^{-2} in CTRL are absent in north-central Oklahoma because of the lack of simulated storms there (Figs. 4d–f and 7b). Conversely, CTRL exhibits strong, persistent helicity tracks in the southern portion of the state, where the model was able to initiate some of the

observed storms while overestimating their intensity (Figs. 4d–f and 7b). As a consequence of the forecast improvements in northwest Oklahoma documented in all the base 3DVAR assimilation experiments (Fig. 5), the respective simulated helicity tracks there (Figs. 7c–f) also exhibit noticeable improvements when evaluated against the NSSL rotation tracks in Fig. 7a. In particular, all assimilation experiments appear to favor supercells in north-central Oklahoma. Among these tracks in northern Oklahoma, all assimilation experiments produce a distinct track northwest of the Oklahoma City metro area (storm highlighted by the horizontal black line in Figs. 3c–e), which arguably appears broadly consistent with the long-track, EF-5 El Reno tornado (e.g., Tanamachi et al. 2015; Houser et al. 2015). In terms of strength, the RAD + OKLMA simulation produces the strongest helicity track northwest of Oklahoma City (Fig. 7e). None of the simulations showed tracks that would be consistent with the EF-3 tornado near Canton, Oklahoma (labeled as "CNT" in Fig. 7a).

The base experiments assimilating radar and/or lightning data (Table 1) all produced rainfall amounts that remained within the ranges of the stage-IV rainfall accumulation estimates (i.e., ≤50–60 mm, Fig. 8). No significant wet biases are present (not shown), unlike the majority of the forecast days analyzed in F15, which used the simple nudging technique of F12a. As documented earlier in Fig. 5, because RAD (and, by extension, RAD + OKLMA) is able to initiate the observed convection earlier than OKLMA, the 5- and 10-mm accumulated precipitation contours extend farther west, and thus appear in better accord with the stage-IV rainfall estimates (Figs. 8a,c,d). The accumulated rainfall in Fig. 8 reveal, however, one noteworthy limitation common to all the simulations; namely, none were able to produce the observed two nearby parallel lines of heavier rainfall exceeding 20 mm oriented southwest–northeast near central Oklahoma. Rather, the assimilation experiments produced similar rainfall totals in the north-central portion of the state. The time sequences of radar reflectivity fields in both the observations and the model (Figs. 4 and 5) revealed that this is caused in part by the tendency for the model to produce supercells moving faster than observed and with a storm motion vector directed more toward the north (e.g., Clark et al. 2012).

To provide a metric to quantify the performance of accumulated precipitation estimates from the DA experiments in the telescoped domain of Fig. 8, neighborhood-based fractions skill scores (Roberts and Lean 2008) relative to the stage-IV observations were computed for CTRL and all the base DA experiments for neighborhood radii ranging from 1 to 45 km (i.e., point based up to 15 grid points). This skill score was selected because it is an attractive measure of skill on convection-allowing grids (Mittermaier et al. 2013). In contrast to the neighborhood-based equitable threat score (ETS; Clark et al. 2010), the fractions skill score provides a quantitative measure of goodness and usefulness, which adds to the understanding of true forecast skill. Because of the large displacement errors in the accumulated precipitation relative to the observations seen in all the DA runs (Fig. 8), the skill scores are not deemed "useful" (i.e., <0.5; Roberts and Lean 2008) even for relatively large neighborhood radii (i.e., 30 and 45 km) and for sufficiently small accumulated precipitation thresholds (i.e., ≤5 mm; Fig. 9). Note that it is indeed feasible to achieve useful scores (>0.5) when the neighborhood radii are allowed to exceed 48 km (not shown). These were not considered, however, because of the relatively small size of the telescoped domain in Fig. 8 and because this did not change the qualitative aspect of the analysis below. Overall, the skill scores in Fig. 9 corroborate the qualitative analysis of the accumulated precipitation fields in Fig. 8: Although all DA experiments fail to reproduce the accumulated precipitation maxima in central Oklahoma, the faster, more broadly distributed development of precipitation in the RAD-based experiments results in systematically slightly larger skill scores than those of the LDA runs at hour 1 and later in the forecast, except at forecast hour 2 (Fig. 9). The skill scores of all DA experiments show a slight improvement over CTRL overall, except at hour 4. Note, however, that the improvements in skill scores are likely limited by errors in storm motion, and so may not fully reflect the arguably larger qualitative improvements to the forecasts. Given the overall similarity in rainfall skill scores in all DA experiments (Fig. 9), it appears that despite the significant differences in storm structures documented earlier in Figs. 3–5, the type of DA does not make much difference in terms of short-term forecasts of accumulated rainfall.

5. Summary

An efficient method for assimilating total lightning data information within a cloud-scale three-dimensional variational technique (or 3DVAR) has been developed using the ARPS 3DVAR system running on the WRF-ARW model. This study describes the method and evaluates results from assimilating lightning and/or radar data for the tornado outbreak on 24–25 May 2011. The philosophy behind this 3DVAR lightning data assimilation (LDA) method follows the basic concept of the nudging (direct insertion) method presented in F12a and subsequently tested in F14 and F15. At observed 2D lightning locations, the technique imposes an increase in water vapor mass toward saturation within a confined

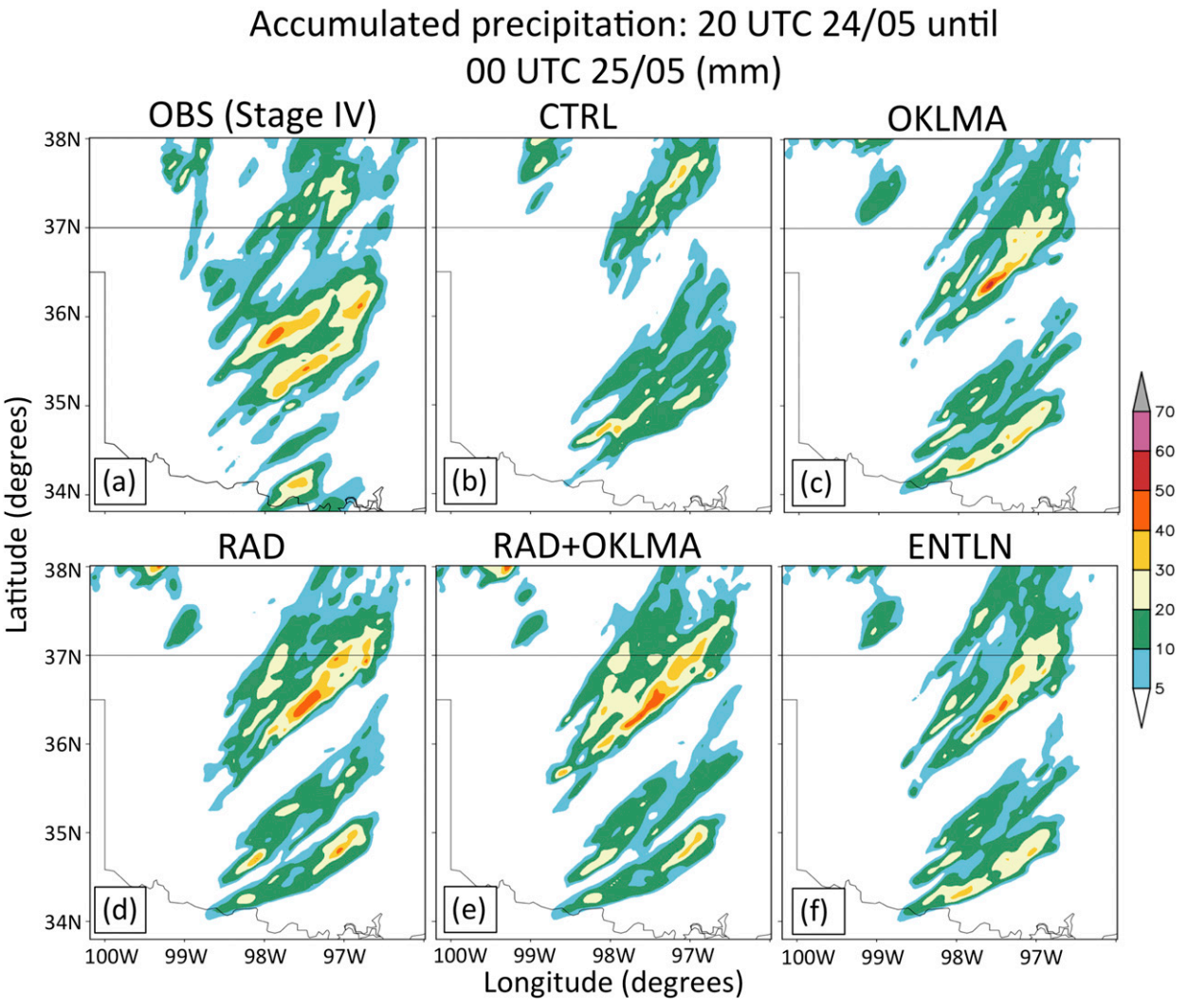

FIG. 8. Horizontal cross sections of accumulated precipitation fields (in mm) starting at 2000 UTC 24 May and ending at 0000 UTC 25 May 2011 over the geographical area of Fig. 2 for (a) the stage-IV data interpolated onto the local 3-km domain, (b) CTRL, (c) OKLMA, (d) RAD, (e) RAD + OKLMA, and (f) ENTLN.

layer to locally increase the virtual potential temperature perturbation, and hence, thermal buoyancy (Houze 1993; Braun 2002; Fierro et al. 2012b).

Assimilating either radar or lightning data produced better forecasts than were produced by the control experiment, which assimilated neither type of data. These forecast improvements include radar reflectivity fields, helicity tracks, and accumulated precipitation amounts that are more consistent with observations, particularly northwest of the Oklahoma City metropolitan area. When only radar reflectivity and radial velocity are assimilated, the improvements during the first 30–45 min of simulation (forecast) are better overall than the improvements from assimilating lightning data alone. This is because the radar assimilation runs initiate storms earlier than the LDA runs do, and so depict the initial storms more accurately, with higher skill scores for the amount and location of accumulated precipitation, especially early in the forecast. The earlier merger in RAD was partially traced back to the small cutoff reflectivity threshold (15 dBZ) typically used to exclude nonmeteorological echoes from the 3DVAR analysis. When a larger reflectivity threshold was used (45 dBZ), the analysis and subsequent short-term forecast were very similar to those of the LDA.

At the 1-h forecast time, however, assimilating either the OK-LMA or the ENTLN lightning data reproduces storm-scale structures in better agreement with the observed storms than the structures produced by assimilating radar data alone. In particular, the LDA storms are characterized by isolated strong rotating updrafts with well-defined supercell characteristics including hook echo appendages, V-shaped reflectivity

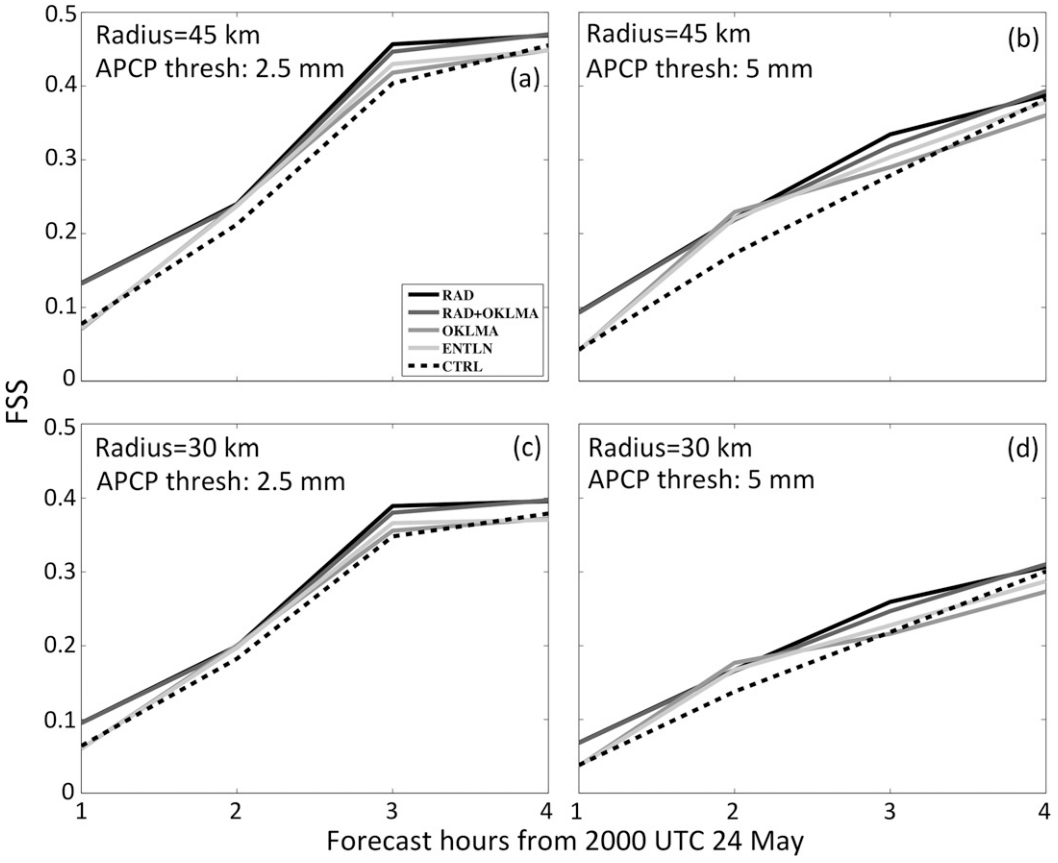

FIG. 9. Fractions skill scores (FSS) of the simulated hourly accumulated precipitation fields relative to the stage-IV observations within the telescoped domain shown in Fig. 4 for forecasts starting at 2000 UTC 24 May and ending at 0000 UTC 25 May 2011 for the CTRL run and the four base data assimilation experiments listed in Table 1. The FSS using a neighborhood radius of 45 km are shown for an hourly accumulated precipitation threshold of (a) 2.5 and (b) 5 mm. (c),(d) As in (a),(b), but for a neighborhood radius of 30 km.

cores, and mesocyclonic rotations collocated with the hook echo and main updraft. Because the storms in OKLMA initiate and develop later than in RAD, the individual supercells merge later in the forecast in the LDA runs, behavior more consistent with that of the observed storms.

Assimilating a combination of radar and lightning data produces better short-term forecasts than are produced by assimilating either radar or lightning data alone, as the model then resolves individual supercell structures more accurately. This is caused by the forecast simultaneously benefiting from the earlier development of the hydrometeor fields by the radar assimilation/cloud analysis and the more targeted updraft forcing from the LDA.

Additional sensitivity experiments (not shown) demonstrated that these results generally held when the Thompson et al. (2004) microphysics scheme was employed in lieu of the Hong and Lim (2006) single-moment 6-class scheme (WSM6) used in this study. The main differences worth documenting are that the storms simulated with the Thompson scheme tended generally to exhibit more isolated reflectivity cores characterized by reflectivity maxima exceeding observed values by as much as 10 dB.

This study also documents an advantage of assimilating lightning data within the 3DVAR framework over the simple nudging scheme of F12a, in that the 3DVAR method could impose larger increases in water vapor mass at a single time. In the present case, this enabled convection to develop faster and improved the representation of the supercellular convection in the short-term forecasts. In F12a, F14, and F15, q_v had to be increased in small increments over a shallow layer, because the sudden introduction of too much mass into the model via direct insertion occasionally resulted in mass–wind imbalance and, ultimately, in computational instability.

In summary, despite a slower development of storm size relative to the assimilation of radar data, the improvements in the placement and evolution of the convection over the control experiment when two-dimensional

lightning densities were assimilated remain noteworthy. This result is particularly encouraging for regions characterized by limited coverage of the WSR-88D network, such as mountainous areas or over oceans, or due to temporary loss of a radar. Further refinements of this LDA scheme will consider selected regions of the United States characterized by either ''good'' versus ''poor'' radar coverage, to determine optimal weights that balance the value added by lightning data against the value added by radar data. Weights could for instance be dynamic, to be modified in real time when the assimilated data sources temporarily change, such as by the loss of a critical radar.

Note that other methods for addressing the loss of a radar are possible. Gao et al. (2016) developed a new assimilation package, now being tested, that introduces ensemble information into this 3DVAR system, so that even if only radial velocity data are assimilated, all model variables are adjusted based on ensemble covariances. Although the LDA described here provides better storm-scale detail than provided by surface-based precipitation methods, future work should address present limitations of the LDA, as well. For instance, (i) the density rate cutoff thresholds used to activate the LDA miss lower flash rate storms in the domain during the assimilation and (ii) the use of a fixed top height to saturate grid columns ignores seasonal and geographical variations. Further research could also evaluate whether, at observed lightning locations, adjusting both the potential temperature and vapor mixing ratio profiles toward the environmental most unstable moist adiabat adds value to the forecast and further hastens the initiation of the observed convection. The rationale would be that the moist adiabat represents a direct linkage between the bulk local total lightning and the vertical profile of updraft buoyancy (e.g., MacGorman et al. 1989).

Although the flash or source density data herein were interpolated onto the original resolution of the model grid (i.e., $3 \times 3\,\mathrm{km}^2$), adapting this LDA method to pseudo-GLM resolutions (e.g., $8 \times 8\,\mathrm{km}^2$) is straightforward. When GLM data become available, hopefully by late 2016, future studies will place emphasis on the assimilation of pseudo-GLM flash extent density data coupled with some of the aforementioned refinements to the LDA method.

Acknowledgments. The authors thank Ami Arthur for providing the NSSL three-dimensional NMQ radar mosaic data. The authors also gratefully acknowledge Brandon Smith (NSSL) who generated the NSSL rotation track analyses that the authors adapted in Fig. 7a. Thanks also go out to Bill Callahan, Stan Heckman, and Jim Anderson from Earth Networks for providing the ENTLN total lightning data. Funding was provided by NOAA/Office of Oceanic and Atmospheric Research under NOAA–University of Oklahoma Cooperative Agreement NA11OAR4320072, U.S. Department of Commerce. This work was further supported by the National Oceanic and Atmospheric Administration (NOAA) of the U.S. Department of Commerce under Grant NOAA-OAR-CIPO-2014-2003893. The simulations were conducted on the NOAA HPC ''Jet'' resources housed in Boulder, Colorado. Auxiliary computer resources were provided by the Oklahoma Supercomputing Center for Education and Research (OSCER) hosted at the University of Oklahoma. The authors would also like to acknowledge Dave Jorgensen and three anonymous reviewers, whose suggestions helped improve the quality of the manuscript.

REFERENCES

Aksoy, A., D. C. Dowell, and C. Snyder, 2009: A multicase comparative assessment of the ensemble Kalman filter for assimilation of radar observations. Part I: Storm-scale analyses. *Mon. Wea. Rev.*, **137**, 1805–1824, doi:10.1175/2008MWR2691.1.

Albers, S. C., J. A. McGinley, D. L. Birkenheuer, and J. R. Smart, 1996: The Local Analysis and Prediction System (LAPS): Analyses of clouds, precipitation, and temperature. *Wea. Forecasting*, **11**, 273–287, doi:10.1175/1520-0434(1996)011<0273:TLAAPS>2.0.CO;2.

Alexander, G. D., J. A. Weinman, V. Karyampudi, W. S. Olson, and A. C. L. Lee, 1999: The effect of assimilating rain rates derived from satellites and lightning on forecasts of the 1993 Superstorm. *Mon. Wea. Rev.*, **127**, 1433–1457, doi:10.1175/1520-0493(1999)127<1433:TEOARR>2.0.CO;2.

Allen, B. J., E. R. Mansell, D. C. Dowell, and W. Deierling, 2016: Assimilation of pseudo-GLM data using the ensemble Kalman filter. *Mon. Wea. Rev.*, **144**, 3465–3486, doi:10.1175/MWR-D-16-0117.1.

Baldwin, M. E., and K. E. Mitchell, 1997: The NCEP hourly multisensor U.S. precipitation analysis for operations and GCIP research. Preprints, *13th Conf. on Hydrology*, Long Beach, CA, Amer. Meteor. Soc., 54–55.

Benjamin, S. G., and Coauthors, 2004: An hourly assimilation–forecast cycle: The RUC. *Mon. Wea. Rev.*, **132**, 495–518, doi:10.1175/1520-0493(2004)132<0495:AHACTR>2.0.CO;2.

Boccippio, D. J., K. L. Cummins, H. J. Christian, and S. J. Goodman, 2001: Combined satellite- and surface-based estimation of the intracloud–cloud-to-ground lightning ratio over the continental United States. *Mon. Wea. Rev.*, **129**, 108–122, doi:10.1175/1520-0493(2001)129<0108:CSASBE>2.0.CO;2.

Braun, S. A., 2002: A cloud-resolving simulation of Hurricane Bob (1991): Storm structure and eyewall buoyancy. *Mon. Wea. Rev.*, **130**, 1573–1592, doi:10.1175/1520-0493(2002)130<1573:ACRSOH>2.0.CO;2.

Brewster, K., 2002: Recent advances in diabatic initialization of a non-hydrostatic numerical model. Preprints, *19th Conf. on Weather Analysis and Forecasting/15th Conf. on Numerical Weather Prediction/21st Conf. on Severe Local Storms*, San Antonio, TX, Amer. Meteor. Soc., J6.3. [Available online at https://ams.confex.com/ams/SLS_WAF_NWP/techprogram/paper_47414.htm.]

Carey, L. D., and S. A. Rutledge, 1998: Electrical and multiparameter radar observations of a severe hailstorm. *J. Geophys. Res.*, **103**, 13 979–14 000, doi:10.1029/97JD02626.

Caumont, O., V. Ducrocq, É. Wattrelot, G. Jaubert, and S. Pradier-Vabre, 2010: 1D+3DVar assimilation of radar reflectivity data: A proof of concept. *Tellus*, **62A**, 173–187, doi:10.1111/j.1600-0870.2009.00430.x.

Chang, D.-E., J. A. Weinman, C. A. Morales, and W. S. Olson, 2001: The effect of spaceborne microwave and ground-based continuous lightning measurements on forecasts of the 1998 Groundhog Day storm. *Mon. Wea. Rev.*, **129**, 1809–1833, doi:10.1175/1520-0493(2001)129<1809:TEOSMA>2.0.CO;2.

Chen, F., Z. Janjić, and K. Mitchell, 1997: Impact of atmospheric surface-layer parameterizations in the new land-surface scheme of the NCEP mesoscale Eta model. *Bound.-Layer Meteor.*, **85**, 391–421, doi:10.1023/A:1000531001463.

Clark, A. J., M. Xue, and M. L. Weisman, 2010: Neighborhood-based verification of precipitation forecasts from convection-allowing NCAR WRF Model simulations and the operational NAM. *Wea. Forecasting*, **25**, 1495–1509, doi:10.1175/2010WAF2222404.1.

——, and Coauthors, 2012: An overview of the 2010 Hazardous Weather Testbed Experimental Forecast Program Spring Experiment. *Bull. Amer. Meteor. Soc.*, **93**, 55–74, doi:10.1175/BAMS-D-11-00040.1.

Deierling, W., and W. A. Petersen, 2008: Total lightning activity as an indicator of updraft characteristics. *J. Geophys. Res.*, **113**, D16210, doi:10.1029/2007JD009598.

Dudhia, J., 1989: Numerical study of convection observed during the winter monsoon experiment using a mesoscale two-dimensional model. *J. Atmos. Sci.*, **46**, 3077–3107, doi:10.1175/1520-0469(1989)046<3077:NSOCOD>2.0.CO;2.

Evensen, G., 1994: Sequential data assimilation with a nonlinear quasi-geostrophic model using Monte Carlo methods to forecast error statistics. *J. Geophys. Res.*, **99**, 10 143–10 162, doi:10.1029/94JC00572.

——, 2003: The ensemble Kalman filter: Theoretical formulation and practical implementation. *Ocean Dyn.*, **53**, 343–367, doi:10.1007/s10236-003-0036-9.

Fierro, A. O., and J. M. Reisner, 2011: High-resolution simulation of the electrification and lightning of Hurricane Rita during the period of rapid intensification. *J. Atmos. Sci.*, **68**, 477–494, doi:10.1175/2010JAS3659.1.

——, M. S. Gilmore, E. R. Mansell, L. J. Wicker, and J. M. Straka, 2006: Electrification and lightning in an idealized boundary-crossing supercell simulation of 2 June 1995. *Mon. Wea. Rev.*, **134**, 3149–3172, doi:10.1175/MWR3231.1.

——, E. Mansell, C. Ziegler, and D. MacGorman, 2012a: Application of a lightning data assimilation technique in the WRF-ARW Model at cloud-resolving scales for the tornado outbreak of 24 May 2011. *Mon. Wea. Rev.*, **140**, 2609–2627, doi:10.1175/MWR-D-11-00299.1.

——, E. J. Zipser, M. A. LeMone, J. M. Straka, and J. Simpson, 2012b: Tropical oceanic hot towers: Need they be undilute to transport energy from the boundary layer to the upper troposphere effectively? An answer based on trajectory analysis of a simulation of a TOGA COARE convective system. *J. Atmos. Sci.*, **69**, 195–213, doi:10.1175/JAS-D-11-0147.1.

——, J. Gao, C. Ziegler, E. R. Mansell, D. R. MacGorman, and S. Dembek, 2014: Evaluation of a cloud scale lightning data assimilation technique and a 3DVAR method for the analysis and short-term forecast of the 29 June 2012 derecho event. *Mon. Wea. Rev.*, **142**, 183–202, doi:10.1175/MWR-D-13-00142.1.

——, A. J. Clark, E. R. Mansell, D. R. MacGorman, S. Dembek, and C. Ziegler, 2015: Impact of storm-scale lightning data assimilation on WRF-ARW precipitation forecasts during the 2013 warm season over the contiguous United States. *Mon. Wea. Rev.*, **143**, 757–777, doi:10.1175/MWR-D-14-00183.1.

Gao, J., and D. J. Stensrud, 2012: Assimilation of reflectivity data in a convective-scale, cycled 3DVAR framework with hydrometeor classification. *J. Atmos. Sci.*, **69**, 1054–1065, doi:10.1175/JAS-D-11-0162.1.

——, M. Xue, A. Shapiro, and K. K. Droegemeier, 1999: A variational method for the retrieval of three-dimensional wind fields from dual-Doppler radars. *Mon. Wea. Rev.*, **127**, 2128–2142, doi:10.1175/1520-0493(1999)127<2128:AVMFTA>2.0.CO;2.

——, ——, K. Brewster, and K. K. Droegemeier, 2004: A three-dimensional variational data assimilation method with recursive filter for single-Doppler radar. *J. Atmos. Oceanic Technol.*, **21**, 457–469, doi:10.1175/1520-0426(2004)021<0457:ATVDAM>2.0.CO;2.

——, and Coauthors, 2013: A real-time weather-adaptive 3DVAR analysis system for severe weather detections and warnings. *Wea. Forecasting*, **28**, 727–745, doi:10.1175/WAF-D-12-00093.1.

——, C. Fu, J. Kain, and D. J. Stensrud, 2016: OSSEs for an ensemble 3DVAR data assimilation system with radar observations of convective storms. *J. Atmos. Sci.*, **73**, 2403–2426, doi:10.1175/JAS-D-15-0311.1.

Ge, G., J. Gao, K. A. Brewster, and M. Xue, 2010: Effects of beam broadening and Earth curvature in radar data assimilation. *J. Atmos. Oceanic Technol.*, **27**, 617–636, doi:10.1175/2009JTECHA1359.1.

——, ——, and M. Xue, 2012: Diagnostic pressure equation as a weak constraint in a storm-scale three-dimensional variational radar data assimilation system. *J. Atmos. Oceanic Technol.*, **29**, 1075–1092, doi:10.1175/JTECH-D-11-00201.1.

Godinez, H. C., J. M. Reisner, A. O. Fierro, S. R. Guimond, and J. Kao, 2012: Determining key model parameters of rapidly intensifying Hurricane Guillermo (1997) using the ensemble Kalman filter. *J. Atmos. Sci.*, **69**, 3147–3171, doi:10.1175/JAS-D-12-022.1.

Goodman, S. J., and Coauthors, 2013: The GOES-R Geostationary Lightning Mapper (GLM). *Atmos. Res.*, **125–126**, 34–49, doi:10.1016/j.atmosres.2013.01.006.

Griffin, E. M., T. J. Schuur, D. M. MacGorman, M. R. Kumjian, and A. O. Fierro, 2014: A polarimetric and electrical analysis of the overland reintensification of Tropical Storm Erin (2007). *Mon. Wea. Rev.*, **142**, 2321–2344, doi:10.1175/MWR-D-13-00360.1.

Gurka, J. J., T. J. Schmit, T. M. Renkevens, M. M. Gunshor, and J. Li, 2006: 2006 update on baseline instruments for the GOES-R series. *Atmospheric and Environmental Remote Sensing Data Processing and Utilization II: Perspective on Calibration/Validation Initiatives and Strategies*, A. H. L. Huang and H. J. Bloom, Eds., International Society for Optical Engineering (SPIE Proceedings, Vol. 6301), Proc. SPIE 6301H, doi:10.1117/12.683701.

Hong, S.-Y., and J.-O. J. Lim, 2006: The WRF single-moment microphysics scheme (WSM6). *J. Korean Meteor. Soc.*, **42**, 129–151.

Houser, J. L., H. B. Bluestein, and J. C. Snyder, 2015: Rapid-scan, polarimetric, Doppler radar observations of tornadogenesis and tornado dissipation in a tornadic supercell: The ''El Reno, Oklahoma'' storm of 24 May 2011. *Mon. Wea. Rev.*, **143**, 2685–2710, doi:10.1175/MWR-D-14-00253.1.

Houtekamer, P. L., and H. Mitchell, 1998: Data assimilation using an ensemble Kalman filter technique. *Mon. Wea. Rev.*, **126**, 796–811, doi:10.1175/1520-0493(1998)126<0796:DAUAEK>2.0.CO;2.

Houze, R. A., 1993: *Cloud Dynamics.* Academic Press, 573 pp.

Hu, M., M. Xue, and K. Brewster, 2006a: 3DVAR and cloud analysis with WSR-88D level-II data for the prediction of the Fort Worth, Texas, tornadic thunderstorms. Part I: Cloud analysis and its impact. *Mon. Wea. Rev.*, **134**, 675–698, doi:10.1175/MWR3092.1.

——, ——, J. Gao, and K. Brewster, 2006b: 3DVAR and cloud analysis with WSR-88D level-II data for the prediction of the Fort Worth, Texas, tornadic thunderstorms. Part II: Impact of radial velocity analysis via 3DVAR. *Mon. Wea. Rev.*, **134**, 699–721, doi:10.1175/MWR3093.1.

Janjić, Z. I., 1994: The step-mountain eta coordinate model: Further developments of the convection, viscous sublayer, and turbulence closure schemes. *Mon. Wea. Rev.*, **122**, 927–945, doi:10.1175/1520-0493(1994)122<0927:TSMECM>2.0.CO;2.

Jones, C. D., and B. Macpherson, 1997a: A latent heat nudging scheme for the assimilation of precipitation data into an operational mesoscale model. *Meteor. Appl.*, **4**, 269–277, doi:10.1017/S1350482797000522.

——, and ——, 1997b: Sensitivity of the limited area model to the assimilation of precipitation estimates derived from lightning data. UKMO Forecasting Research Tech. Rep. 212, 11 pp.

Kain, J. S., S. R. Dembeck, S. J. Weiss, J. L. Case, J. J. Levit, and R. A. Sobash, 2010: Extracting unique information from high-resolution forecast models: Monitoring selected fields and phenomena every time step. *Wea. Forecasting*, **25**, 1536–1542, doi:10.1175/2010WAF2222430.1.

Kosiba, K., J. Wurman, P. Robinson, C. Schwartz, D. Burgess, E. Mansell, and D. Dawson II, 2012: Mobile radar observations and damage assessment of the 24 May 2011, Canton Lake, OK tornado. *26th Conf. on Severe Local Storms*, Nashville, TN, Amer. Meteor. Soc., P102. [Available online at https://ams.confex.com/ams/26SLS/webprogram/Paper211754.html.]

Kuhlman, K. M., C. L. Zielger, E. R. Mansell, D. R. MacGorman, and J. M. Straka, 2006: Numerically simulated electrification and lightning of the 29 June 2000 STEPS supercell storm. *Mon. Wea. Rev.*, **134**, 2734–2757, doi:10.1175/MWR3217.1.

Lakshmanan, V., T. Smith, G. Stumpf, and K. Hondl, 2007: The Warning Decision Support System–Integrated Information. *Wea. Forecasting*, **22**, 596–612, doi:10.1175/WAF1009.1.

Lopez, P., and P. Bauer, 2007: "1D+4DVAR" assimilation of NCEP Stage-IV radar and gauge hourly precipitation data at ECMWF. *Mon. Wea. Rev.*, **135**, 2506–2524, doi:10.1175/MWR3409.1.

Lund, N. R., D. R. MacGorman, T. J. Schuur, M. J. Biggerstaff, and W. D. Rust, 2009: Relationships between lightning location and polarimetric radar signatures in a small mesoscale convective system. *Mon. Wea. Rev.*, **137**, 4151–4170, doi:10.1175/2009MWR2860.1.

MacGorman, D. R., and W. D. Rust, 1998: *The Electrical Nature of Storms*. Oxford University Press, 422 pp.

——, D. W. Burgess, V. Mazur, W. D. Rust, W. L. Taylor, and B. C. Johnson, 1989: Lightning rates relative to tornadic storm evolution on 22 May 1981. *J. Atmos. Sci.*, **46**, 221–251, doi:10.1175/1520-0469(1989)046<0221:LRRTTS>2.0.CO;2.

——, W. D. Rust, P. Krehbiel, W. Rison, E. Bruning, and K. Wiens, 2005: The electrical structure of two supercell storms during STEPS. *Mon. Wea. Rev.*, **133**, 2583–2607, doi:10.1175/MWR2994.1.

——, and Coauthors, 2008: TELEX: The Thunderstorm Electrification and Lightning Experiment. *Bull. Amer. Meteor. Soc.*, **89**, 997–1013, doi:10.1175/2007BAMS2352.1.

——, I. R. Apostolakopoulos, N. R. Lund, N. W. S. Demetriades, M. J. Murphy, and P. R. Krehbiel, 2011: The timing of cloud-to-ground lightning relative to total lightning activity. *Mon. Wea. Rev.*, **139**, 3871–3886, doi:10.1175/MWR-D-11-00047.1.

Mansell, E. R., 2014: Storm-scale ensemble Kalman filter assimilation of total lightning flash data. *Mon. Wea. Rev.*, **142**, 3683–3695, doi:10.1175/MWR-D-14-00061.1.

——, C. L. Ziegler, and D. R. MacGorman, 2007: A lightning data assimilation technique for mesoscale forecast models. *Mon. Wea. Rev.*, **135**, 1732–1748, doi:10.1175/MWR3387.1.

Marchand, M., and H. Fuelberg, 2014: Assimilation of lightning data using a nudging method involving low-level warming. *Mon. Wea. Rev.*, **142**, 4850–4871, doi:10.1175/MWR-D-14-00076.1.

Marécal, V., and J.-F. Mahfouf, 2002: Four-dimensional variational assimilation of total column water vapor in rainy areas. *Mon. Wea. Rev.*, **130**, 43–58, doi:10.1175/1520-0493(2002)130<0043:FDVAOT>2.0.CO;2.

——, and ——, 2003: Experiments on 4D-Var assimilation of rainfall data using an incremental formulation. *Quart. J. Roy. Meteor. Soc.*, **129**, 3137–3160, doi:10.1256/qj.02.120.

Mellor, G. L., and T. Yamada, 1982: Development of turbulence closure model for geophysical fluid problems. *Rev. Geophys. Space Phys.*, **20**, 851–875, doi:10.1029/RG020i004p00851.

Mittermaier, M., N. Roberts, and S. A. Thompson, 2013: A long-term assessment of precipitation forecast skill using the Fractions Skill Score. *Meteor. Appl.*, **20**, 176–186, doi:10.1002/met.296.

Mlawer, E., S. Taubman, P. Brown, M. Iacono, and S. Clough, 1997: Radiative transfer for inhomogeneous atmospheres: RRTM, a validated correlated-*k* model for the longwave. *J. Geophys. Res.*, **102**, 16 663–16 682, doi:10.1029/97JD00237.

Papadopoulos, A., T. G. Chronis, and E. N. Anagnostou, 2005: Improving convective precipitation forecasting through assimilation of regional lightning measurements in a mesoscale model. *Mon. Wea. Rev.*, **133**, 1961–1977, doi:10.1175/MWR2957.1.

Park, S. K., and L. Xu, Eds., 2013: *Data Assimilation for Atmospheric, Oceanic and Hydrologic Applications (Vol. II)*. Springer-Verlag, 730 pp., doi:10.1007/978-3-642-35088-7.

Pessi, A. T., and S. Businger, 2009: The impact of lightning data assimilation on a winter storm simulation over the North Pacific Ocean. *Mon. Wea. Rev.*, **137**, 3177–3195, doi:10.1175/2009MWR2765.1.

Purser, R. J., W.-S. Wu, D. F. Parrish, and N. M. Roberts, 2003a: Numerical aspects of the application of recursive filters to variational statistical analysis. Part I: Spatially homogeneous and isotropic Gaussian covariances. *Mon. Wea. Rev.*, **131**, 1524–1535, doi:10.1175//1520-0493(2003)131<1524:NAOTAO>2.0.CO;2.

——, ——, ——, and ——, 2003b: Numerical aspects of the application of recursive filters to variational statistical analysis. Part II: Spatially inhomogeneous and anisotropic general covariances. *Mon. Wea. Rev.*, **131**, 1536–1548, doi:10.1175//2543.1.

Rison, W., R. J. Thomas, P. R. Krehbiel, T. Hamlin, and J. A. Harlin, 1999: GPS-based three-dimensional lightning mapping system: Initial observations. *Geophys. Res. Lett.*, **26**, 3573–3576, doi:10.1029/1999GL010856.

Roberts, N. M., and H. W. Lean, 2008: Scale-selective verification of rainfall accumulations from high-resolution forecasts of convective events. *Mon. Wea. Rev.*, **136**, 78–97, doi:10.1175/2007MWR2123.1.

Skamarock, W. C., and J. B. Klemp, 2008: A time-split nonhydrostatic atmospheric model for weather research and forecasting applications. *J. Comput. Phys.*, **227**, 3465–3485, doi:10.1016/j.jcp.2007.01.037.

Smith, T., and K. L. Elmore, 2004: The use of radial velocity derivatives to diagnose rotation and divergence. *11th Conf. on Aviation, Range, and Aerospace*, Hyannis, MA, Amer. Meteor.

Soc., P5.6. [Available online at https://ams.confex.com/ams/11aram22sls/techprogram/paper_81827.htm.]

——, and Coauthors, 2016: Multi-Radar Multi-Sensor (MRMS) severe weather and aviation products: Initial operating capabilities. *Bull. Amer. Meteor. Soc.*, **97**, 1617–1630, doi:10.1175/BAMS-D-14-00173.1.

Stensrud, D. J., and J. Gao, 2010: Importance of horizontally inhomogeneous environmental initial conditions to ensemble storm-scale radar data assimilation and very short-range forecasts. *Mon. Wea. Rev.*, **138**, 1250–1272, doi:10.1175/2009MWR3027.1.

——, and Coauthors, 2009: Convective-scale Warn-On-Forecast system: A vision for 2020. *Bull. Amer. Meteor. Soc.*, **90**, 1487–1499, doi:10.1175/2009BAMS2795.1.

Tanamachi, R. L., P. L. Heinselman, and L. J. Wicker, 2015: Impacts of a storm merger on the 24 May 2011 El Reno, Oklahoma, tornadic storm. *Wea. Forecasting*, **30**, 501–524, doi:10.1175/WAF-D-14-00164.1.

Thomas, R. J., P. R. Krehbiel, W. Rison, S. J. Hunyady, W. P. Winn, T. Hamlin, and J. Harlin, 2004: Accuracy of the Lightning Mapping Array. *J. Geophys. Res.*, **109**, D14207, doi:10.1029/2004JD004549.

Thompson, G., R. M. Rasmussen, and K. Manning, 2004: Explicit forecasts of winter precipitation using an improved bulk microphysics scheme. Part I: Description and sensitivity analysis. *Mon. Wea. Rev.*, **132**, 519–542, doi:10.1175/1520-0493(2004)132<0519:EFOWPU>2.0.CO;2.

Weiss, S. A., D. R. MacGorman, and K. M. Calhoun, 2012: Lightning in the anvils of supercell thunderstorms. *Mon. Wea. Rev.*, **140**, 2064–2079, doi:10.1175/MWR-D-11-00312.1.

Wiens, K. C., S. A. Rutledge, and S. A. Tessendorf, 2005: The 29 June 2000 supercell observed during STEPS. Part II: Lightning and charge structure. *J. Atmos. Sci.*, **62**, 4151–4177, doi:10.1175/JAS3615.1.

Wurman, J., and K. Kosiba, 2013: Finescale radar observations of tornado and mesocyclone structures. *Wea. Forecasting*, **28**, 1157–1174, doi:10.1175/WAF-D-12-00127.1.

Xue, M., and Coauthors, 2001: The Advanced Regional Prediction System (ARPS)—A multi-scale nonhydrostatic atmospheric simulation and prediction tool. Part II: Model physics and applications. *Meteor. Atmos. Phys.*, **76**, 143–165, doi:10.1007/s007030170027.

——, D. Wang, J. Gao, K. Brewster, and K. K. Droegemeier, 2003: The Advanced Regional Prediction System (ARPS), storm-scale numerical weather prediction and data assimilation. *Meteor. Atmos. Phys.*, **82**, 1393–170, doi:10.1007/s00703-001-0595-6.

Zhang, F., 2005: Dynamics and structure of mesoscale error covariance of a winter cyclone estimated through short-range ensemble forecasts. *Mon. Wea. Rev.*, **133**, 2876–2893, doi:10.1175/MWR3009.1.

——, Y. Weng, J. A. Sippel, Z. Meng, and C. H. Bishop, 2009: Cloud-resolving hurricane initialization and prediction through assimilation of Doppler radar observations with an ensemble Kalman filter. *Mon. Wea. Rev.*, **137**, 2105–2125, doi:10.1175/2009MWR2645.1.

Zhang, J., F. Carr, and K. Brewster, 1998: ADAS cloud analysis. Preprints, *12th Conf. on Numerical Weather Prediction*, Phoenix, AZ, Amer. Meteor. Soc., 185–188.

——, and Coauthors, 2011: National Mosaic and Multi-Sensor QPE (NMQ) System: Description, results, and future plans. *Bull. Amer. Meteor. Soc.*, **92**, 1321–1338, doi:10.1175/2011BAMS-D-11-00047.1.

Zhuang, Z., N. Yussouf, and J. Gao, 2016: The analyses and forecasts of 24 May 2011 Oklahoma tornadic supercell storms using ensemble of 3DVAR system. *Adv. Atmos. Sci.*, **33**, 544–558, doi:10.1007/s00376-015-5072-0.

CORRIGENDUM

ALEXANDRE O. FIERRO

Cooperative Institute for Mesoscale Meteorological Studies, University of Oklahoma, and NOAA/OAR/National Severe Storms Laboratory, Norman, Oklahoma

JIDONG GAO AND CONRAD L. ZIEGLER

NOAA/National Severe Storms Laboratory, Norman, Oklahoma

KRISTIN M. CALHOUN

Cooperative Institute for Mesoscale Meteorological Studies, University of Oklahoma, and NOAA/OAR/National Severe Storms Laboratory, Norman, Oklahoma

EDWARD R. MANSELL AND DONALD R. MACGORMAN

NOAA/National Severe Storms Laboratory, Norman, Oklahoma

(Manuscript received 28 March 2017, in final form 12 April 2017)

In all the lightning data assimilation (LDA) experiments of Fierro et al. (2016, hereafter F16), it is stated that, outside the observed lightning areas, the pseudo-observations for water vapor mass (q_v) were not created because these grid points are considered as non-updraft areas. This implied that pseudo-q_v outside the lightning areas were treated as missing values, which was the original intent. In the 3DVAR package, however, the missing pseudo-q_v outside the lightning areas were inadvertently assigned a zero innovation instead of a missing value. Because of this, all LDA-based experiments were assimilating zero innovations for q_v outside the lightning areas, forcing the analysis for q_v close to the background values there. Consequently, the information of pseudo-q_v inside the lightning areas (set to the saturation q_v with respect to liquid) cannot be spread out to the nonlightning areas, constraining the impact of the LDA. While setting the q_v innovations to zero in nonlightning areas could also be a valid approach to assimilate lightning, the fact that the radar data assimilation experiment (RAD) treated the radial winds as missing values outside reflectivity areas (i.e., no radial wind observations for $\mathrm{dBZ} \leq 15$–20) lead to inequitable comparisons between the original RAD and LDA experiments.

To illustrate this, an auxiliary experiment treating pseudo-q_v as missing values outside lightning areas and using the same horizontal decorrelation length scales R as in F16 (Table 1) was performed and shown in Fig. 3e. As can now be seen, when correctly assigning missing pseudo-q_v values in nonlightning areas, the 3DVAR analysis spreads the impact of the pseudo-q_v from inside the lightning areas (set to saturation q_v) to nonlightning areas (Fig. 6d). This has the main effect of producing an analysis and 1-h forecast that are arguably worse than the original RAD experiment (Figs. 3d,e). To produce results that are qualitatively comparable to the original LDA experiments (i.e., more targeted updraft cores), R must therefore be set to smaller values as illustrated by Figs. 3c and 3f and Figs. 6b and 6e for the OKLMA experiment (Table 1). Figures 3g and 6f show that when the same small R values are chosen in

Corresponding author: Alexandre O. Fierro, alex.fierro@noaa.gov

DOI: 10.1175/MWR-D-17-0082.1

RAD, it is able to produce isolated convective cells in the analysis as well. Last, for these same smaller R values, Fig. 3h confirms that when the LDA is applied in tandem with RAD, the 1-h forecast is further improved relative to when only lightning (Fig. 3f) or radar data (Fig. 3g) are assimilated. While using $R \leq 10$ km may be optimal for the LDA, it can be arguably said that larger R values (>10 km) would benefit radial velocity assimilation (Figs. 3d,g). That is because radial velocity has a larger representative horizontal scale than the lightning data. Consequently, to effectively assimilate both types of observations, a multiscale approach, wherein different length scales are used for different types of observations, should be envisaged.

Despite this ambiguity, the additional experiments herein confirm that the general proof-of-concept of the 3DVAR LDA method in F16 remains valid. It is relevant to also clarify that the vertical decorrelation length scale used in all the experiments is 4 grid points, and not 12 km as incorrectly stated in F16.

REFERENCE

Fierro, A. O., J. Gao, C. L. Ziegler, K. M. Calhoun, E. R. Mansell, and D. R. MacGorman, 2016: Assimilation of flash extent data in the variational framework at convection-allowing scales: Proof-of-concept and evaluation for the short-term forecast of the 24 May 2011 tornado outbreak. *Mon. Wea. Rev.*, **144**, 4373–4393, doi:10.1175/MWR-D-16-0053.1.

TABLE 1. The left column lists the nomenclature/abbreviations used for the simulations/experiments described herein. The second column from the left briefly describes the type of experiments. The second column from the right indicates the type of data that were assimilated, with "dBZ" standing for radar reflectivity and "Vr" for radial velocity. The right column shows which model variable(s) is (are) impacted by the respective assimilation experiments with the symbols used to identify those variables bearing their usual meaning. For convenience, the first three rows list the original control run (CTRL), original lightning data assimilation experiment using the Oklahoma Lightning Mapping Array (OK-LMA) data, and the original radar data assimilation experiment (RAD). The first (second) value of R corresponds to the horizontal decorrelation length scale used during the first (second) 10-iteration pass of the 3DVAR analysis.

Experiment	Description	Data assimilated	Model variables impacted
CTRL	Original control run	None	None
OKLMA	Original lightning assimilation run	OK-LMA flash extent density rates	q_v (LCL-15 km)
RAD	Original radar data assimilation run	Vr and dBZ	q_r, q_g, q_i, q_s, q_h, u, v, w, θ
H24 OKLMA	Lightning assimilation run with R = 24, 12 km	OK-LMA flash extent density rates	q_v (LCL-15 km)
H6 OKLMA	Lightning assimilation run with R = 6, 3 km	OK-LMA flash extent density rates	q_v (LCL-15 km)
H6 RAD	Radar data assimilation run with R = 6, 3 km	Vr and dBZ	q_r, q_g, q_i, q_s, q_h, u, v, w, θ
H6 RAD+OKLMA	Lightning + radar data assimilation run with R = 6, 3 km	Vr and dBZ, OK-LMA flash extent density rates.	q_v (LCL-15 km), q_r, q_g, q_i, q_s, q_h, u, v, w, θ

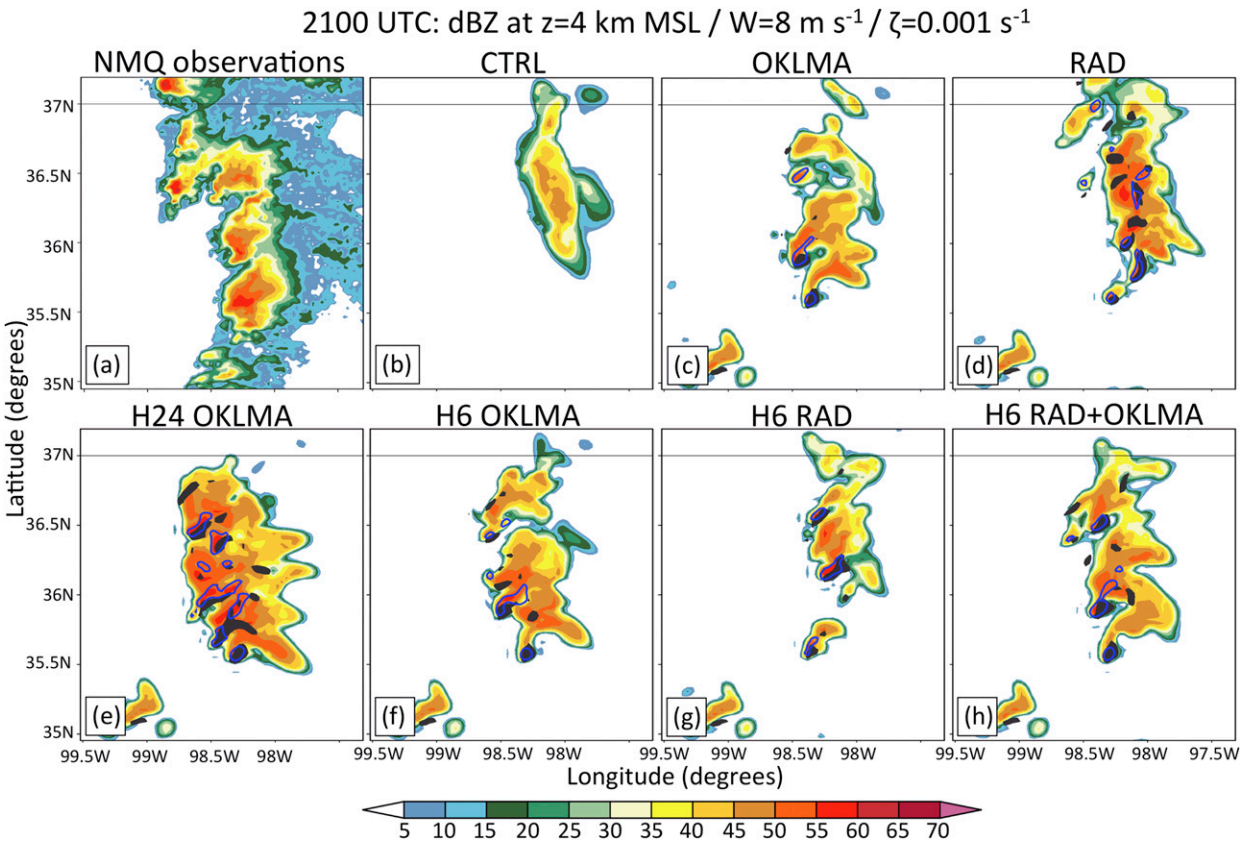

FIG. 3. Horizontal cross sections at 2100 UTC (1-h forecast) at $z = 4$ km MSL overlain with the 8 m s^{-1} vertical velocities (blue contour) and relative vertical vorticities of 10^{-3} s^{-1} (solid black) for (a) the NMQ observations, (b)–(d) selected original base experiments in F16, and (e)–(h) additional experiments described in Table 1.

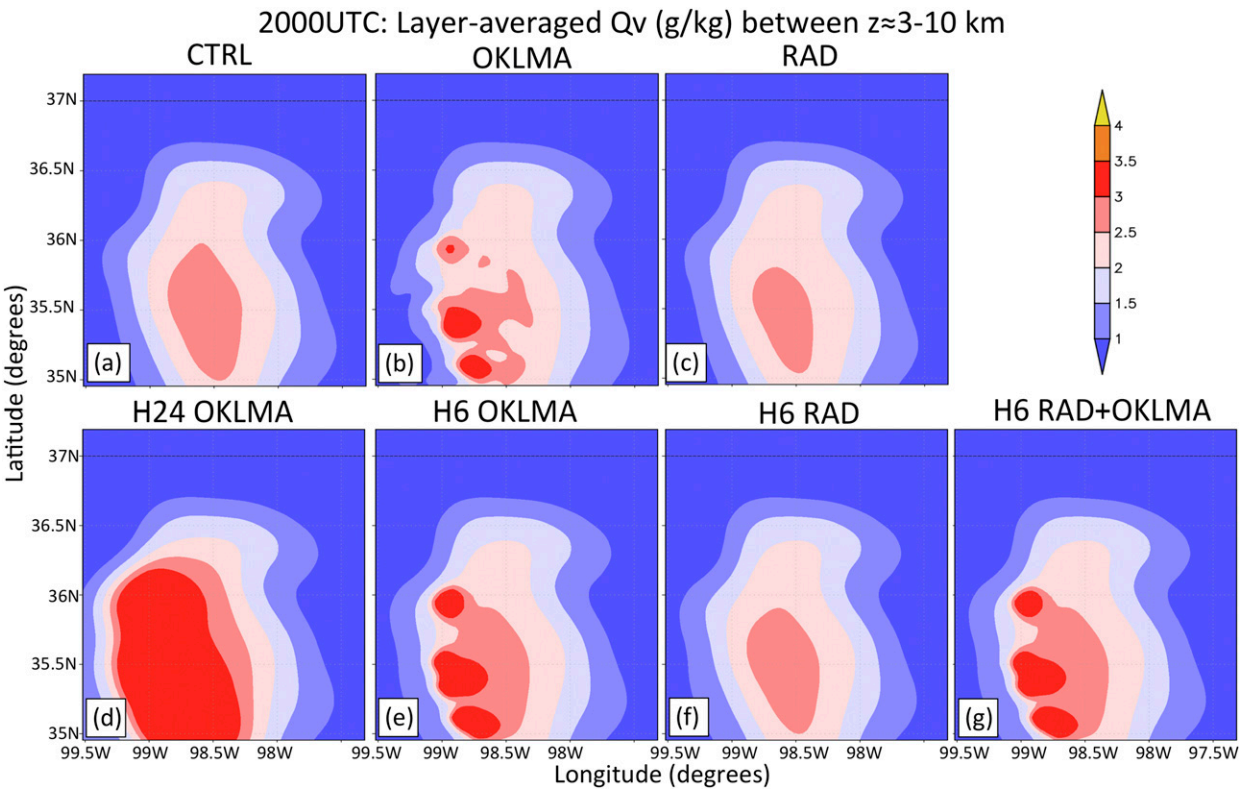

FIG. 6. Layer-averaged water vapor mass (q_v) between $z \approx 3$ and 10 km MSL at 2000 UTC. Results are shown from left to right for the original (a) CTRL, (b) OKLMA, and (c) RAD experiments followed by (d)–(g) the additional experiments described in Table 1.